Modelling for three dimensional coalescence of two bubbles

Han, R.; Li, s; Zhang, A. M.; Wang, Qian

DOI:
10.1063/1.4953175

Document Version
Peer reviewed version

Citation for published version (Harvard):
Han, R, Li, S, Zhang, AM & Wang, Q 2016, 'Modelling for three dimensional coalescence of two bubbles', *Physics of Fluids*, vol. 28, 062104. https://doi.org/10.1063/1.4953175

Modelling for three dimensional coalescence of two bubbles

R. Han,[1] S. Li,[1] A. M. Zhang,[1,*] Q. X. Wang[2]

[1] College of Shipbuilding Engineering, Harbin Engineering University, Harbin, P.R. China

[2] School of Mathematics, University of Birmingham, Birmingham B15 2TT, United Kingdom

Abstract: This paper is concerned with the three dimensional interaction and coalescence of two bubbles subject to buoyancy and the dynamics of the subsequent joined bubble using the boundary integral method (BIM). An improved density potential method is implemented to control the mesh quality. It helps to avoid the numerical instabilities which occur after coalescence. Numerical convergence tests are conducted in terms of mesh sizes and time steps. The 3D numerical model agrees well with an axisymmetric BIM model for axisymmetric cases as well as experimental results captured by high-speed camera. The bubble jetting, interaction and coalescence of the two bubbles depend on the maximum bubble radii, the centre distance between two bubbles at inception and the angle β between the centre line and the direction of buoyancy. We investigate coalescence of two bubbles for $\beta = 0$, $\pi/4$, and $\pi/2$, respectively, and at various centre distances at inception. Numerical results presented include the bubble and jet shapes, the velocity and pressure fields surrounding the bubbles, as well as the time histories of bubble volumes, jet velocities and positions of centroid of the bubble system.

Key words: Bubble dynamics; Three dimensional coalescence; Boundary integral method; Improved density potential control

1. Introduction

Studies on bubble dynamics are associated with many problems, such as underwater explosion bubbles (Cole, 1948; Klaseboer et al., 2005), cavitation bubbles (Brennen, 1995), and airgun bubbles for seabed exploration (Cox et al., 2004). The above mentioned fields involve multiple-bubble interactions which has aroused many researchers' interest.

The basic case is the interaction between two equally sized bubbles without gravity. Two bubbles are incepted simultaneously and repel each other in the expansion phase. During the collapse phase, the bubbles tend to form jets towards each other (Mitchell and Hammitt, 1973; Blake et al., 1993). The dynamics of each bubble is the same as that of the one near a plane rigid wall placed midway between the two bubbles (Tomita et al., 1990; Cui et al., 2016). In fact, dynamics in the bubble-bubble interaction relates to the relative size of bubbles, the distance between two bubbles and the difference in the bubble inception time (Fong et al., 2009; Han et al.,

* Corresponding author. Tel./Fax: +86 0451 82518296.
E-mail address: zhangaman@hrbeu.edu.cn (A. M. Zhang).

2015a). Many researchers have investigated the interaction between two bubbles and the results obtained have illustrated the complex nature of the interaction. The key experimental studies on two-bubble interaction are those of Lauterborn (1982), Tomita et al. (1990), Bremond et al. (2006), Fong et al. (2009), Chew et al. (2011), Hsiao et al. (2013) and Han et al. (2015a). In the work by Fong et al. (2009), the interaction between two similarly sized bubbles was investigated and different bubble behaviors were classified in a graph. Jet towards, jet away, coalescence and a behavior termed the 'catapult effect' were observed. There are also some numerical studies on two-bubble interaction (Blake et al., 1993; Bremond et al., 2006; Fong et al., 2009; Hsiao et al., 2013; Han et al., 2015a; Han et al., 2015b). In the previous works, the high-speed jet for bubbles with phase difference or size difference has attracted much attention. There are few studies focused on the coalescence of two bubbles, especially in a gravity field.

Two-bubble coalescence occurs if two bubbles are quite close to each other (Lal and Menon, 1996, Fong et al., 2009; Chew et al. 2011; Cui et al., 2016). Earlier examination on coalescence of two bubbles was found in Lal and Menon (1996). They carried out small scale experiments with two underwater explosion bubbles in a water tank. They conducted experiments for both in-phase and out-of-phase explosions. The jets formed inside the coalesced bubble are not visible in the experiment. Fong et al. (2009) observed the 'swelling' of the middle section of the resulting coalesced bubble (spark-generated bubble), followed by two jets formed along the centre line and contact at the mid-point. Similar phenomena are observed by Cui et al. (2016). They also stated that the coalesced bubble sides are associated with smaller curvature radii and should collapse faster according to a proportional relationship between radius and Rayleigh collapse time. However, buoyancy is not significant in the above experimental studies, which plays an important role in underwater explosion/airgun bubble dynamics.

Rungsiyaphornrat et al. (2003) simulated the coalescence of two explosion bubbles using the axisymmetric boundary integral method. They put forward the coalescence criterion, and bubble shapes and periods of oscillation were predicted well, compared to the experimental work of Lal and Menon (1996). Obviously, there are situations when the axisymmetric BIM have limitations. If the effect of buoyancy is not negligible, only the coalescence of two bubbles when the angle between the centre line and the direction of buoyancy is $\beta = 0$ can be simulated using the axisymmetric BIM. However, the bubble dynamics are related to the type of two-bubble configuration (various β), the strength of buoyancy and the distance between two inception centres. As far as we are concerned, there's no such research on the effects of the above parameters on the dynamics of coalescence. A three dimensional model is believed to be essential to study the effects of the above factors on the coalescence of two bubbles.

In the present study, a three dimensional model is established to simulate the coalescence of two bubbles by using the boundary integral method. The topology treatment involved in the three dimensional coalescence is quite complex, which causes problems for the investigation on the coalescence phenomenon. An improved density potential method is implemented to avoid the numerical instabilities after coalescence. The validation of the numerical model is confirmed by comparison with axisymmetric BIM model and experiment captured by high-speed camera. The convergence tests are also conducted. At last, we investigate the dynamics of the coalescence of two bubbles in three types of configurations: the angle between the centre line and the direction of gravity is $\beta = 0$, $\pi/4$, and $\pi/2$, respectively. We examine the bubble shape, jet velocity and Kelvin impulse etc., in terms of the buoyancy parameter and the inter-bubble distance. Some new features of two-bubble coalesecence are observed and discussed in detail.

2. Physical and mathematical model

It is assumed that the fluid surrounding the bubbles is inviscid and incompressible, and the flow irrotational. Thus, the velocity potential φ satisfies the Laplace's equation:

$$\nabla^2 \varphi = 0 . \tag{2.1}$$

The boundary integral method is used to investigate bubble dynamics. Application of Green's theorem yields the solution of Laplace's equation in integral form as:

$$c(\boldsymbol{r})\varphi(\boldsymbol{r}) = \iint_S \left(\frac{\partial \varphi(\boldsymbol{q})}{\partial n} \frac{1}{|\boldsymbol{r}-\boldsymbol{q}|} - \varphi(\boldsymbol{q}) \frac{\partial}{\partial n}\left(\frac{1}{|\boldsymbol{r}-\boldsymbol{q}|} \right) \right) dS(\boldsymbol{q}) , \tag{2.2}$$

where $\boldsymbol{r}$ and $\boldsymbol{q}$ are the field point and the source point, respectively, c is the solid angle at the field point $\boldsymbol{r}$, $\boldsymbol{n}$ is the outward normal of the bubble surfaces, and S is the boundary of the fluid domain.

Consider the interaction and coalescence of two bubbles, which are assumed adiabatic. The surface tension is ignored because the Weber number associated with the cases in this paper can be estimated as $O(10^4)$. The internal pressure of the two bubbles, P_1 and P_2, thus satisfy

$$P_i = P_{i0} \left(\frac{V_{i0}}{V_i} \right)^{\lambda} , \qquad i = 1, 2, \tag{2.3}$$

where V_i and $V_{\mathrm{i}0}$ are the transient and initial volumes of the two bubble, respectively, and λ is the ratio of the specific heats of the gas, which equal 1.25 for underwater explosions with TNT (Cole, 1948). A Cartesian coordinate system O-xyz is adopted with its origin at the centre of the centre line, the z-axis parallel to the direction of buoyancy. The bubble centres at inception are on the plane $y = 0$. The dimensional distance between two inception centres is d_{bb}.

The kinematic boundary condition and dynamic boundary conditions on the bubble surface are as follows:

$$\frac{\mathrm{d}\boldsymbol{r}}{\mathrm{d}t}=\nabla\varphi, \tag{2.4a}$$

$$\frac{\mathrm{d}\varphi}{\mathrm{d}t}=\frac{\left|\nabla\varphi\right|^2}{2}+\frac{P_\infty}{\rho}-\frac{P_i}{\rho}-gz, \tag{2.4b}$$

where P_∞ is the ambient pressure on the plane of the bubble center at inception, ρ is the fluid density, and g is the acceleration of gravity.

Following the work by Rungsiyaphornrat et al. (2003), the internal gases reach rapidly equilibrium after coalescence as compared to the external liquid flow responding to changes in the bubble pressure, which is assumed to happen instantly. The heat transfer from the internal gases to the external liquid is ignored within this short time, and thus the internal energy of the system remains unchanged,

$$\left(n_1+n_2\right)c_vT_c=n_1c_vT_1+n_2c_vT_2, \tag{2.5}$$

where n_1 and n_2 are the amount of moles of gases in bubbles 1 and 2 respectively, c_v the heat capacity at constant volume of the gas, T_1 and T_2 the temperatures of the bubbles before coalescence, and T_c the temperature of the joined bubble. The gas inside the bubble behaves according to the ideal gas law, i.e.

$$P_{c0}V_{c0}=\left(n_1+n_2\right)\Re T_c, \tag{2.6a}$$

$$P_1V_1=n_1\Re T_1, \qquad P_2V_2=n_2\Re T_2, \tag{2.6b, c}$$

where P_{c0} is the stating pressure of the joined bubble, and $\Re$ is the universal gas constant. The initial internal pressure of the joined bubble is obtained from (2.5) and (2.6)

$$P_{c0}V_{c0}=P_1V_1+P_2V_2, \tag{2.7}$$

We neglect the small difference in the total bubble volume just prior to and after coalescence,

$$V_{c0}=V_1+V_2. \tag{2.8}$$

With the initial internal pressure P_{c0} and volume V_{c0} for the joined bubble, its pressure can be calculated in the subsequent computation through (2.3).

We choose the maximum equivalent bubble radius that a single bubble would attain in an infinite field, R_m, as the reference length, liquid density ρ as the reference density, and the ambient pressure P_∞ as the reference pressure. The following dimensionless variables are introduced

$$\gamma_{bb}=\frac{d_{bb}}{R_m},\quad \varepsilon=\frac{P_0}{P_\infty},\quad \delta=\sqrt{\frac{\rho g R_m}{P_\infty}},\quad t_*=\frac{t}{R_m}\sqrt{\frac{P_\infty}{\rho}}. \tag{2.9}$$

All the variables are nondimensionalized with the reference scales and expressed using the same variables subsequently, unless otherwise stated explicitly. With the strength parameter ε known, the dimensionless initial radius of bubble R_0 can be obtained through the solution of the following equation (Klaseboer et al., 2005)

$$\varepsilon\left(R_0^{3\lambda}-R_0^3\right)=\left(1-\lambda\right)\left(1-R_0^3\right). \tag{2.10}$$

3. Modelling for 3D bubble coalescence

When the surfaces of two bubbles approach and flat each other, the liquid film between them becomes thinner and thinner and finally may rupture, leading to coalescence. It is difficult to simulate the whole process of coalescence, since the mesh size has to be small compared to the thickness of the thin film. We assume that the coalescence of two bubbles occurs, when the minimum distance between their surfaces satisfies the following condition

$$d_{\min}=\min\left(\left(\boldsymbol{r}_1-\boldsymbol{r}_2\right)\cdot\boldsymbol{n}_1\right)\le\Delta s, \tag{3.1}$$

where $\boldsymbol{r}_1$ and $\boldsymbol{r}_2$ are on the surfaces of bubbles 1 and 2 respectively, $\boldsymbol{n}_1$ is the normal vector at the surface of bubble 1. In the calculations performed in this paper, we choose $\Delta s=0.02$. We denote the minimum distance occurs at the two nodes $\boldsymbol{r}_{O1}$ and $\boldsymbol{r}_{O2}$, respectively. We then perform the numerical coalescence, using two approaches for axisymmetric cases and 3D cases respectively.

3.1. Axisymmetric coalescence

For axisymmetric cases, the mesh around the joining point $\boldsymbol{r}_{O1}$ appears approximately axisymmetric, as shown in Fig. 1. We group the neighbouring nodes to the joining point in various rings, with the first two rings shown in Fig. 1(a).

Then check the distances of the nodes of each ring to the opposite bubble surface. If every node $\boldsymbol{r}_{1\mathrm{K}}$ on ring K satisfies the following inequality but the nodes on ring K+1 do not

$$d_{\min}=\left(\boldsymbol{r}_{1K}-\boldsymbol{r}_2\right)\cdot\boldsymbol{n}_{1K}\le\Delta s, \tag{3.2}$$

ring K is chosen as the coalescence line and the surface enclosed by the line is the coalescence surface.

Fig. 2(a) shows bubble shapes and two coalescence lines just prior to the coalescence and Fig. 2(b) shows coalesced bubble shape and the ‘stitch’ line after coalescence. The coordinates of the nodes on the two coalescence lines are symmetric with respect to the plane x = 0, thus a smooth ‘stitch’ line can be obtained. Fig. 2(b) also shows the amplified local view for the elements around the ‘stitch’ line, and a large size difference between the elements can be found. However,

it has little effect on the subsequent motion of the coalesced bubble.

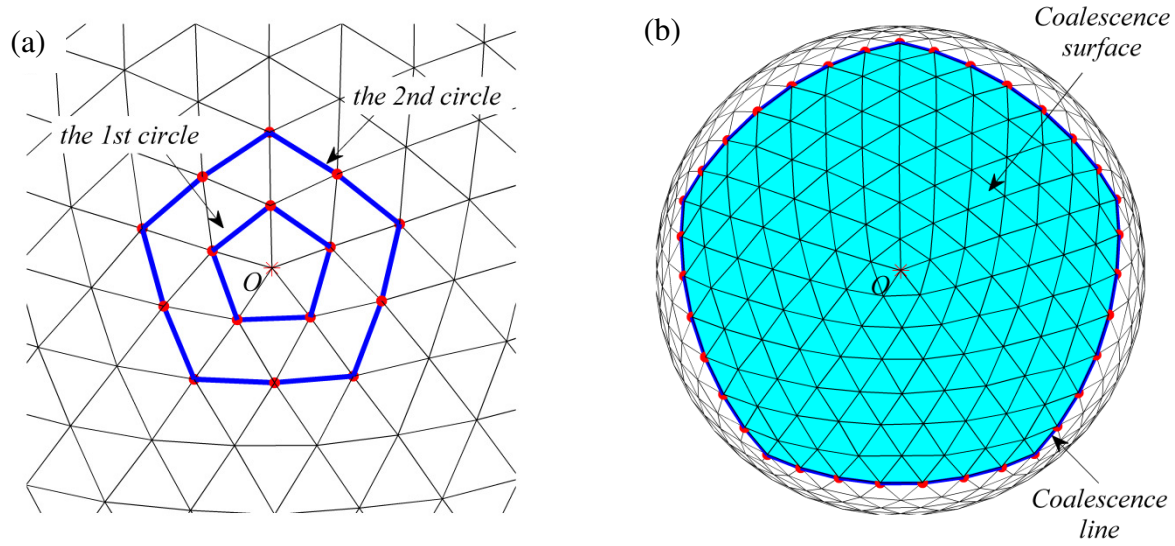

Fig. 1. Finding coalescence line and coalescence surface using the 1st approach. (a) Sketch of the surrounding elements and nodes to the centre O. (b) Sketch of the coalescence surface and coalescence line at the coalescence time. In the computation, the angle between the centre line and the direction of buoyancy is $\beta = 0$ and the inter-bubble distance is $\gamma_{bb} = 0.9$. The simulation parameters are $\varepsilon = 100$, $R_0 = 0.1485$, $\delta = 0$. There are 642 nodes and 1280 elements on each bubble surface.

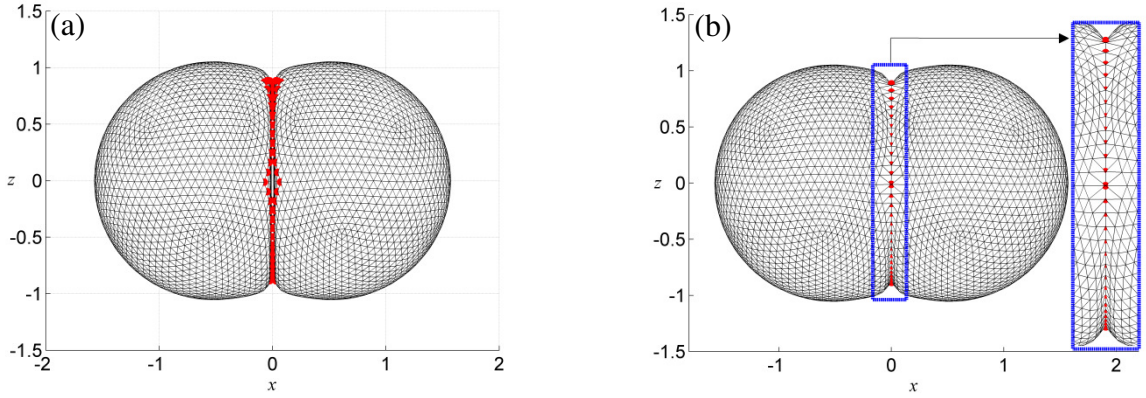

Fig. 2. Topology treatment for the coalescence of two bubbles using the 1st approach. (a) Bubble shapes and two coalescence lines just prior to coalescence. (b) Coalesced bubble shape and the 'stitch' line after coalescence. The angle between the centre line and the direction of buoyancy is $\beta = \pi/2$ and the inter-bubble distance is $\gamma_{bb} = 1.0$. The simulation parameters are $\varepsilon = 50$, $R_0 = 0.1911$, $\delta = 0$. There are 2562 nodes and 5210 elements on each bubble surface.

3.2. 3D coalescence

Consider strong buoyancy effect or there are boundaries near two bubbles, the shape of the

coalescence surface may significantly deviate from a circle or the coordinates of the nodes on the two coalescence lines are not symmetric with respect to the plane of symmetry. The 1st approach cannot apply to the above cases, thus the 2nd approach is given as follows. There are N_1 and N_2 nodes on the surfaces of bubble 1 and bubble 2, respectively. The distance between the nodes of bubble 1 and those of bubble 2 is written as $|\boldsymbol{r}_{ij}| = |\boldsymbol{r}_{1i}-\boldsymbol{r}_{2j}|$ (i = 1, 2,…, N_1; j = 1, 2,…, N_2). When the coalescence criterion (3.1) is satisfied, we consider that the nodes satisfying the conditions $\left|\boldsymbol{r}_{ij}\right| \le c_1 \cdot \Delta s$ and $d_{ij} = \boldsymbol{r}_{ij} \cdot \boldsymbol{n}_{2j} \le c_2 \cdot \Delta s$ (c_1 and c_2 are constants, c_1 = 2.0 ~ 3.0 and c_2 = 2.0 ~ 3.0 are selected to avoid numerical instabilities after coalescence) are in the coalescence surface and should be deleted. The triangular elements where the nodes belong are found automatically, and make up the coalescence surfaces S_1 and S_2. The lines surrounding the surfaces S_1 and S_2 are the coalescence lines l_1 and l_2, respectively. Then, the validity of the coalescence lines should be tested. For example, we sort the nodes on l_1 in a certain direction and it can be judged whether S_1 is surrounded by one curve or not. If more than one curve is found to surround S_1, c_1 and c_2 are increased until there's only one curve surrounding S_1. In fact, the validity of the coalescence lines can be assured in most cases by using the two above conditions. Fig. 3 shows the coalescence line and the coalescence surface obtained using the 2nd approach. It's the same case as shown in Fig. 1, thus the difference between these two approaches can be easily seen. The blue dots in Fig. 3(a) are the nodes satisfying the above conditions. All the elements where the nodes belong are found and make up the coalescence surface coloured blue. The line surrounding the blue surface is the coalescence line. Topology treatment for the coalescence of two bubbles in a horizontal configuration with $\delta = 0.5$ using this approach is illustrated in Fig. 4. Fig. 4(a) shows bubble shapes and two coalescence lines just prior to the coalescence and Fig. 4(b) shows coalesced bubble shape and the 'stitch' line after coalescence. The amplified local view for the elements around the 'stitch' line is also given in Fig. 4(b). There's only a small size difference between the elements, which benefits the accuracy of the 3D model. The topology treatment procedure can be summarized as follows.

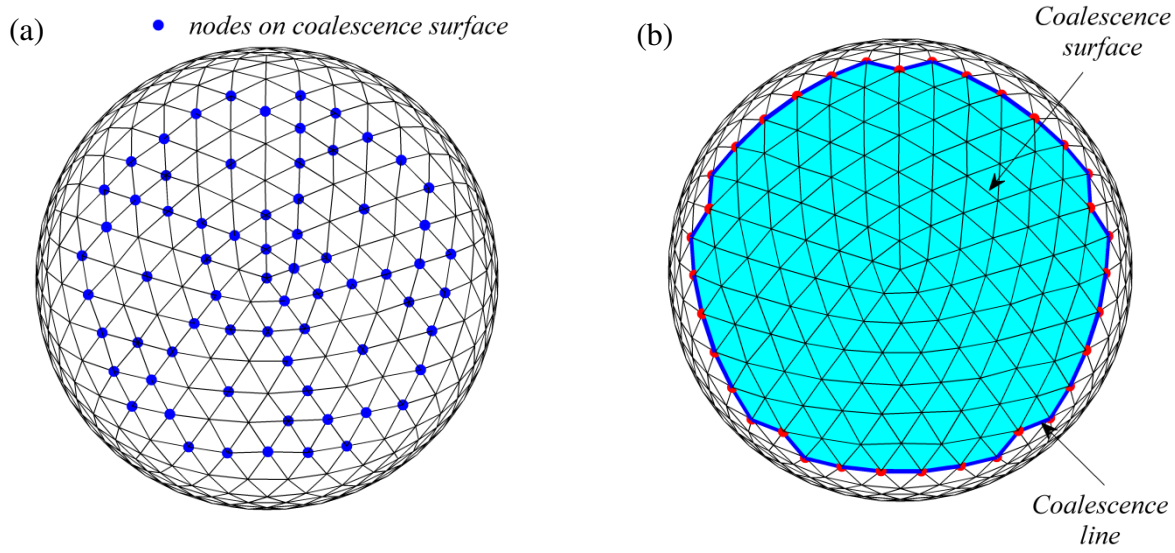

Fig. 3. Finding coalescence line and coalescence surface using the 2nd approach. (a) Sketch of the nodes satisfying $\left|\boldsymbol{r}_{i,j}\right| \le c_1 \cdot \Delta s$ and $d_{i,j} \le c_2 \cdot \Delta s$ (b) Sketch of the coalescence surface and coalescence line at the coalescence time. The same case as shown in Fig. 1.

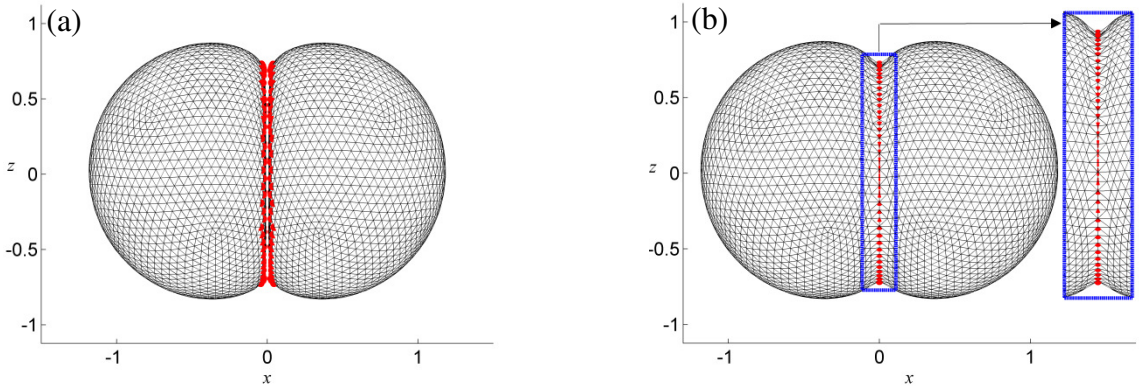

Fig. 4. Topology treatment for the coalescence of two bubbles using the 2nd approach. (a) Bubble shapes and two coalescence lines just prior to coalescence. (b) Coalesced bubble shape and the 'stitch' line after coalescence. The angle between the centre line and the direction of buoyancy is $\beta = \pi/2$ and the inter-bubble distance is $\gamma_{bb} = 1.0$. The simulation parameters are $\varepsilon = 50$, $R_0 = 0.1911$, $\delta = 0.5$. There are 2562 nodes and 5210 elements on each bubble surface.

Pre-coalescence disposal

The nodes $M_1^1, M_2^1, \cdots, M_m^1$ belong to l_1, and $M_1^2, M_2^2, \cdots, M_n^2$ belong to l_2. The numbers of the nodes on l_1 and l_2 are m and n, respectively. At first, the nodes on each line must be sorted in the same direction (clockwise or anticlockwise). Then compare the numbers of the nodes on l_1 and l_2. If $m = n$, turn to the next step. If the numbers of nodes on the two lines do not match, e.g. $m < n$, additional nodes are inserted along the appropriate line segments on l_1 to bring the

numbers to par. After inserting nodes on l_1, nodes are unevenly distributed. Cubic spline interpolation is used to redistribute the nodes.

Coalescence disposal

Now the numbers of the nodes on the two coalescence lines are the same and nodes are evenly distributed. A new set of nodes is then created at the midpoints between the corresponding M_i^1 and M_i^2 nodes. A 'stitch' line is thus obtained. To avoid mesh distortion after the coalescence, the 'stitch' line is smoothed based on the moving least square method.

Mesh and nodes renumbering

The nodes on the coalescence surface and on the coalescence line are all deleted. The elements on the coalescence surface are also deleted. The remaining nodes and the nodes on the 'stitch' line are distributed over the coalesced bubble surface. Then we renumber all the nodes and update the numbers of the nodes belonging to the remaining elements according to the new set of node numbers. At last, the element numbers are updated. Thus the information of the coalesced bubble is obtained.

4. Mesh quality control after coalescence

In the simulation for the coalescence of two bubbles, a smoother should be applied to avoid numerical instabilities like mesh distortion. After jet forms inside the coalesced bubble, the overcrowding of the nodes at the jet tip may occur which leads to a poor quality mesh. A few numerical techniques are thus implemented to solve the above problems. Details are given as below.

4.1. Bubble surface interpolation

The bubble surface is interpolated using a moving least square method following Zhang et al. (2001) and Wang (2005). The coordinate of node *A* is $\boldsymbol{r}_0$ and its surrounding elements need smoothing. A local Cartesian coordinate system, *O*-*XYZ*, is introduced, with its origin *O* at the point *A*, and its *Z*-axis along the normal direction $\boldsymbol{n}_0$. A second order polynomial is implemented for the bubble surface as follows,

$$Z = f(X,Y) = \alpha_1 X^2 + \alpha_2 XY + \alpha_3 Y^2 + \alpha_4 X + \alpha_5 Y + \alpha_6 . \tag{4.1}$$

The coefficients $\alpha_1, \alpha_2 \cdots \alpha_6$ are related to the neighboring nodes within $s_{\max}$ from node *A* and $s_{\max}$ is twice of the average distance from the surrounding nodes to node *A*. *X*, *Y* and *Z* are the coordinates in a local coordinate system. There are N_a nodes near node *A*, and the error function associated with the moving least-square method is thus defined as

$$\mathrm{E}(\alpha_1,\alpha_2,\alpha_3,\alpha_4,\alpha_5,\alpha_6)=\sum_{k=1}^{N_a}W_k[f(X_k,Y_k)-Z_k]^2. \tag{4.2}$$

W_k is the weighted function of node $\boldsymbol{r}_k$. A spline function is chosen as the weighted function as follows

$$W_k=\begin{cases}\dfrac{2}{3}-4\overline{s}^2+4\overline{s}^3 & (\overline{s}\le\dfrac{1}{2})\\ \dfrac{4}{3}-4\overline{s}+4\overline{s}^2-\dfrac{4}{3}\overline{s}^3 & (\dfrac{1}{2}<\overline{s}\le 1)\\ 0 & (\overline{s}>1)\end{cases}, \tag{4.3}$$

where $\overline{s}=\dfrac{s}{s_{\max}}$, $s=|\boldsymbol{r}_0-\boldsymbol{r}_k|$。

The coefficients $\alpha_1,\alpha_2\cdots\alpha_6$ are determined by setting $\dfrac{\partial \mathrm{E}}{\partial\alpha_j}=0$, yielding

$$\sum_{j=1}^{6}A_{ij}\alpha_j=B_i,(i=1,2,\ldots,6), \tag{4.4}$$

where A_{ij} are B_i given as below

$$\begin{gathered}A_{ij}=\sum_{k=1}^{N_a}W_k\zeta_{kj}\zeta_{ki},\qquad B_i=\sum_{k=1}^{N_a}W_kZ_k\zeta_{ki}\\ \left.\begin{gathered}\zeta_{k1}=1,\quad \zeta_{k2}=X_k,\quad \zeta_{k3}=Y_k\\ \zeta_{k4}=X_k^2,\zeta_{k5}=X_kY_k,\zeta_{k6}=Y_k^2\end{gathered}\right\}\quad (k=1,2,\ldots N_a)\end{gathered}. \tag{4.5}$$

The corresponding velocity potential distributed over the bubble surface can be obtained in the same manner.

4.2. Mesh density control

If the true velocity is used to update the bubble surface in the BIM computation, nodes would move from the positions with low velocity potentials to those with high velocity potentials. With such poor quality mesh, obviously, both computational efficiency and accuracy decrease. For axisymmetric BIM model, nodes are evenly distributed by applying cubic spline interpolation, but it's hard to maintain a uniform mesh on the surface of a three dimensional model. To solve the problem, Wang et al. (2003) proposed an elastic mesh technique (EMT) for improving the mesh quality. Based on the idea of the EMT, Zhang et al. (2015) put forward a density potential method (DPM). In the previous works, the bubble surface was advanced with the normal velocity plus an artificial tangential velocity. The tangential velocity in the EMT is obtained by minimizing the total elastic energy stored in each segment of the mesh. While in the work by Zhang et al. (2015), the tangential velocity is constructed by introducing a density potential and the quality of the

mesh is evaluated by the density potential. The mesh nodes can move in tangential directions to any target locations by using DPM, because the selected density potential can be related to not only the mesh size but other factors like the curvature.

For the coalescence problem, a high quality mesh of the bubble surface is maintained by implementing an improved DPM. The theory of the DPM is described as follows. A density potential ψ is introduced and a uniform density field represents a uniform mesh. If the density field is non-uniform, there will be a gathering of nodes around the zone with high density potential. Therefore, the DPM velocity comprising the normal velocity and the calculated tangential velocity is used to update the bubble surface with an 'optimum' mesh in the new time step. An 'optimum' mesh can be obtained by minimizing the variance of ψ. The variance is expressed as $D(\psi)=\int_S \left(\psi - E(\psi)\right)^2 \mathrm{d}s$, where $E(\psi)$ is the mean value of ψ, defined as $E(\psi)=\int_S \psi \mathrm{d}s / S$. The optimum mesh (a uniform mesh) can be obtained by minimizing the variance $D(\psi)$, therefore the derivative of $D(\psi)$ with respect to $\boldsymbol{u}_i = (u_i, v_i, w_i)$ equals 0, yielding

$$\frac{\partial D(\psi)}{\partial u_i} = 0, \quad \frac{\partial D(\psi)}{\partial v_i} = 0, \quad \frac{\partial D(\psi)}{\partial w_i} = 0. \tag{4.6}$$

In the calculation, the normal component of the imaginary DPM velocity must be identical to the true normal velocity ($\boldsymbol{u}_{DPM} \cdot \boldsymbol{n} = \nabla\varphi \cdot \boldsymbol{n}$), which is based on the level set technique (Sussman et al., 1994; Sussman et al., 1999). Then both the evolution of bubble surface and a uniform mesh are maintained. Overall, the DPM velocity $\boldsymbol{u}_{DPM}$ is composed of the imaginary tangential velocity $\boldsymbol{u}_\tau$ and the true normal velocity $\boldsymbol{u}_n$, and can be expressed as

$$\boldsymbol{u}_{DPM} = \boldsymbol{u}_\tau + \boldsymbol{u}_n = \boldsymbol{u}_\tau + \frac{\partial\varphi}{\partial \boldsymbol{n}}. \tag{4.7}$$

To calculate tangential velocity $\boldsymbol{u}_\tau$ of each node on bubble surface, an iterative method is adopted and the iteration procedure is given as below (Zhang et al., 2015)

$$\boldsymbol{u}_\tau^{i+1} = \Im\left\{\boldsymbol{u}_\tau^i + \frac{k}{\Delta t}\nabla\left[\psi\left(\boldsymbol{r} + \Delta t \boldsymbol{u}_{DPM}^i\right)\right]\right\}, \tag{4.8}$$

where the superscript represents the number of iteration, 30 is chosen in the present paper; $\boldsymbol{r}$ is the position vector of node on bubble surface at the moment; the function $\Im(\boldsymbol{x})=\boldsymbol{x}-(\boldsymbol{x}\cdot\boldsymbol{n})\boldsymbol{n}$ projects the vector $\boldsymbol{x}$ onto the tangential plane of the surface; k is the iteration step length factor and k = 0.2. Obviously, nodes will gather around the zone with higher ψ if they are updated

using the tangential velocity obtained by the 2nd term on the right hand. If the density field is uniform, the tangential velocity obtained equals zero.

In this study, the density potential of each node ψ is calculated through the following equation

$$\psi_i = \frac{\Theta_i \cdot \sum_{j=1}^{N_{\text{ele}}} A_{i,j}}{N_{\text{ele}}}, \tag{4.9}$$

where N_{ele} is the number of the elements connected with node i, $A_{i,j}$ is the area of the j^{th} element, and Θ_i is a weight function of node i. The selection of Θ is related to the research object. For the problem in this paper, different weight functions are selected before and after the coalescence to control the mesh quality. Before coalescence occurs, the distance between two bubbles decreases in the expansion phase until the coalescence criterion is satisfied. In order to decrease numerical errors, nodes are expected to gather to the coalescence zone, and the element size is thus smaller than the minimum distance between the two bubbles. Besides, we also consider the curvature κ. Therefore, Θ_i before the coalescence is selected as

$$\Theta_i = \frac{1}{2}\mathrm{N}\left(\frac{1}{\min(d_{i,j})}\right) + \frac{1}{2}\mathrm{N}(\kappa_i), \tag{4.10}$$

where N represents the normalization operator.

Jet forms in the collapse phase of the coalesced bubble. A non-uniform mesh is more suitable for a bubble surface with a varying curvature and a finer mesh should be used for the part of the bubble surface where the curvature is large, such as around the jet surface. Therefore, Θ_i after the coalescence is selected as

$$\Theta_i = \frac{1}{2}\mathrm{N}(\varphi_i) + \frac{1}{2}\mathrm{N}(\kappa_i). \tag{4.11}$$

The DPM velocity $\boldsymbol{u}_{DPM}$ comprising the tangential velocity obtained $\boldsymbol{u}_\tau$ and the true normal velocity $\boldsymbol{u}_n$ is adopted to update the bubble surface, and dynamic boundary condition on the bubble surface (2.4b) is thus rewritten as

$$\frac{\mathrm{d}\varphi}{\mathrm{d}t} = \nabla\varphi \cdot \boldsymbol{u}_{DPM} - \frac{|\nabla\varphi|^2}{2} + \frac{P_\infty}{\rho} - \frac{P_l}{\rho} - gz. \tag{4.12}$$

The comparison of the mesh on the bubble surface just before coalescence is given in Fig. 5. The bubble surface is updated using the real velocity, the hybrid approach velocity (Wang and Manmi, 2014) and the improved DPM velocity, respectively. Before coalescence, there's little difference between Fig. 5(a) and Fig. 5(b), and a uniform mesh is observed. Compared with the

first two frames, there're more nodes gathering on the coalescence surfaces by using an improved DPM, as shown in Fig. 5(c). The non-uniform mesh at the coalescence point is good for the subsequent computation. Obviously, the movement of the nodes on bubble surface can be controlled by using an improved DPM.

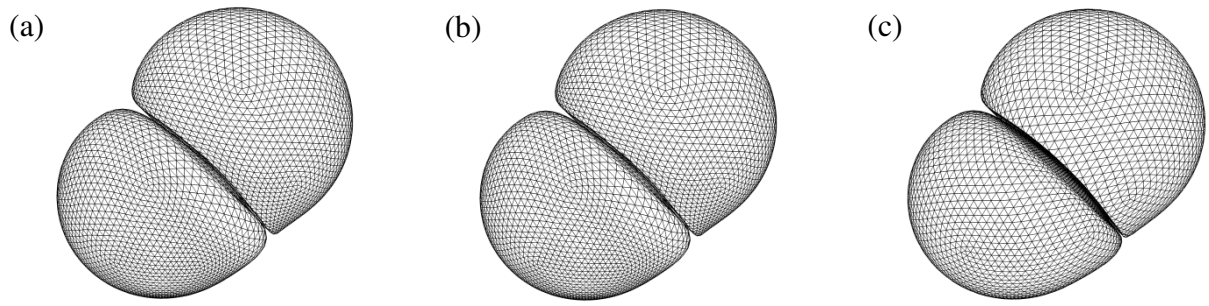

Fig. 5. The comparison of the mesh on the bubble surface at $t_* = 1.08$ (just before coalescence) using (a) the real velocity, (b) the hybrid approach velocity and (c) the improved DPM velocity. In the computation, the angle between the centre line and the direction of buoyancy is $\beta = \pi/4$, and the parameters are $\varepsilon = 50$, $R_0 = 0.1911$, $\gamma_{bb} = 1.0$ and $\delta = 0.5$.

The comparison of the mesh on the bubble surface in the collapse phase is given in Fig. 6. A jet forms at the bubble bottom at this moment. After coalescence, the elements near the 'stitch' line are relatively larger. If the bubble surface is updated using the real velocity, too many nodes are gathering rapidly at the jet tip vicinity and mesh distortion occurs around the 'stitch' line, as shown in Fig. 6(a). This problem can be solved using the hybrid EMT approach. The hybrid EMT approach were applied every 4 time steps. As shown in Fig. 6(b), the mesh quality around the 'stitch' line is well controlled; however, fewer nodes at the tip vicinity may lead to accuracy decrease. Fig. 6(c) shows the mesh on the bubble surface using the improved DPM velocity. A non-uniform mesh is obtained, which is suitable for capturing the jet evolution. Obviously, the jet surface is smoother and with finer mesh than the first two methods.

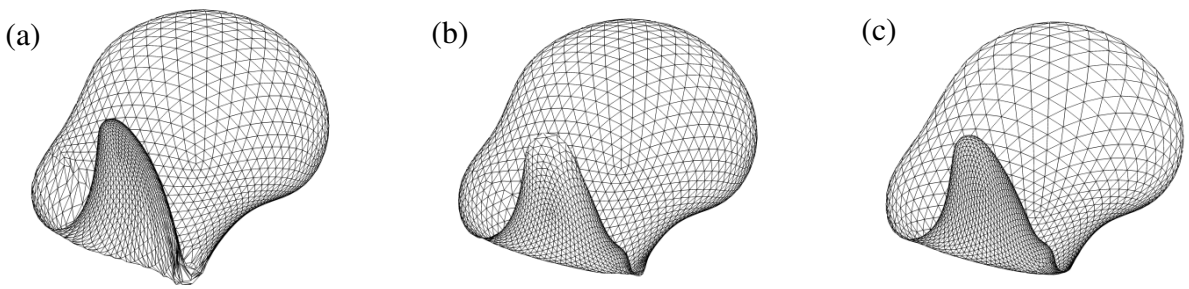

Fig. 6. The comparison of the meshes of the bubble surface at $t_* = 2.15$ using (a) the real velocity,

(b) the hybrid EMT approach velocity and (c) the improved DPM velocity. The same case as shown in Fig. 5.

5. Validation of the numerical model

5.1. Comparison to axisymmetric BIM model and convergence tests

The convergence test of the numerical model has been performed for the case shown in Fig. 1 at various numbers of surface nodes, N = 1002, 1442 and 2562, respectively. The axis connecting initial bubble centres is parallel to the direction of buoyancy (β = 0), and two jets shooting towards are observed in the collapse phase, contacting in the middle without the effect of buoyancy. The bubble shapes at the end of the collapse phase at t_* = 2.30 are illustrated in Fig. 7, compared with the corresponding axisymmetric result (red dashed line). The 3D results are convergent to the mesh size and approach to the axisymmetric result. The presence of more nodes makes better regulation of the jet. N=2562 is selected in the following simulation for accuracy.

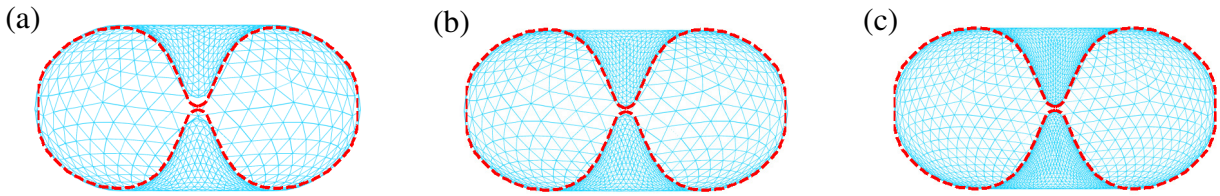

Fig. 7. The bubble shapes at the end of the collapse phase at t_* = 2.30 with various numbers of nodes for the case shown in Fig. 1: (a) N = 1002, (b) N = 1442 and (c) N = 2562, compared with the axisymmetric model (red dashed line).

5.2. Comparison with experiments

The 3D results are compared with the experiment captured by high-speed camera to validate the numerical model. Bubbles are generated via spark discharge in a transparent water tank (500×500×500 mm^3) and the discharge voltage is 300V. Series connection is used to generate in-phase bubble pairs and the angle between the centre line and the direction of buoyancy is $\beta = \pi/2$. In the experiment, the maximum radius of two bubbles is about 10.50mm, and their initiation distance is 5.80mm. In the computation, the dimensionless inter-bubble distance is $\gamma_{bb} = 0.55$ and the parameters used are $\varepsilon = 100, R_0 = 0.1485$. The buoyancy parameter is $\delta = 0.0319$.

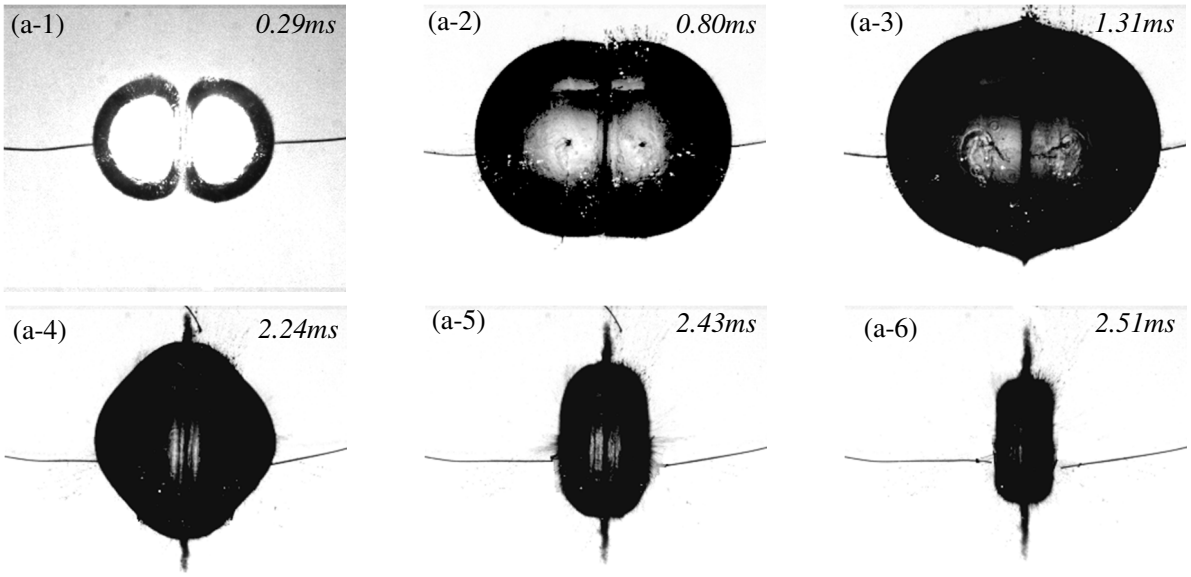

(a)

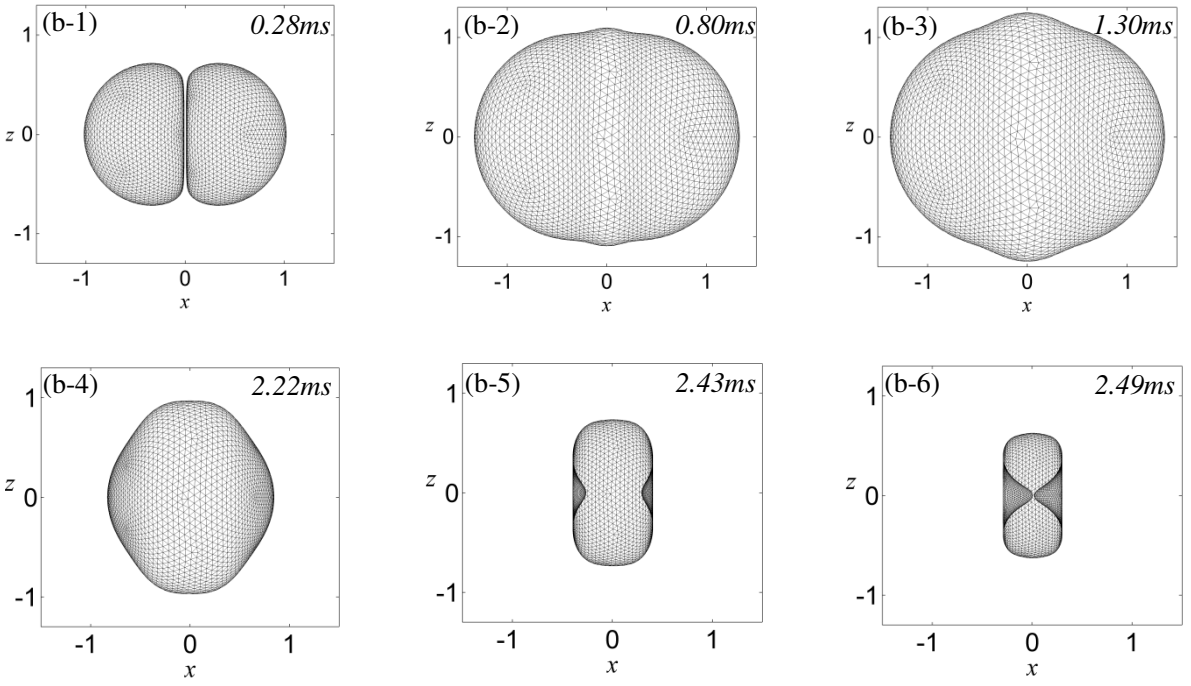

(b)

Fig. 8. Comparison of (a) the experiment with (b) the BIM computation for bubble shapes at various times for the coalescence of two bubbles in a free field. In the computation, the parameters used are $\varepsilon = 100, R_0 = 0.1485, \delta = 0.0319$ and the dimensionless inter-bubble distance measured in the experiment is $\gamma_{bb} = 0.55$. The frame number is placed at the corner of each frame, and its corresponding time is marked in italic font.

Fig. 8 shows the comparison of the experimental and the numerical results for two in-phase equally sized bubbles with weak buoyancy. The bubble shapes are compared at representative

times with slight differences between the experiment and computation. In the experiment, the coalescence doesn't occur instantaneously. The bubble surfaces flatten and form a liquid film between them and the rupture of the liquid film leads to coalescence (see Fig. 8(a-1) - Fig. 8(a-2)). After coalescence, subsequent evolution of the coalesced bubble leads to the swelling of the bubble surface near the coalescence position due to inertia (see Fig. 8(a-3)). Coalescence makes the coalesced bubble elongated along the axis of symmetry, and the elongated ends collapse faster (see Fig. 8(a-4)). In the collapse phase of the coalesced bubble, two jets in contrary direction are formed (see Fig. 8(a-5)). As shown in Fig. 8(a-6), the jets are about to contact in the middle of the coalesced bubble at 2.51ms. In Fig. 8(a-4) - Fig. 8(a-6), a ring surrounding the bubble is observed, because the radial flow outwards from the axis results in the separation of a portion of the coalescence position. The BIM computation is illustrated in Fig. 8(b), and the results show favourable agreement with the experiment. At the first time sequence, the coalescence criterion is satisfied in the numerical simulation and the interfaces between two bubbles become flattened. Similar to Fig. 8(a-3), a swelling of the bubble surface near the coalescence position is reproduced in Fig. 8(b-3). Then bubble comes into the collapse phase. The left and right sides of the coalesced bubble with higher curvature collapse faster (Vogel et al., 1989), thus two jets directed horizontally are produced. Two jets are about to contact at 2.49ms (as shown in Fig. 8(b-6)). In the numerical simulation, coalescence occurs instantaneously and the ring observed in the experiment cannot be obtained.

The energy of the bubble system and the total bubble volume versus time are illustrated in Fig. 9, and coalescence point is marked with a red dashed line. At the coalescence point, we notice a very small 0.03% drop of the total energy and a small 3% difference in the total bubble volume. Fig. 9 also shows that the total energy is always conserved throughout the simulation, and fluctuations of the total energy are within 1%, showing the high accuracy of the present model.

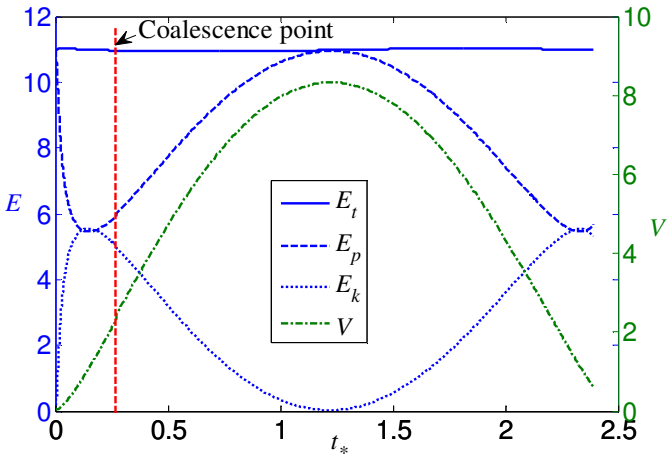

Fig. 9. Time histories of total energy, potential energy, kinetic energy and total bubble volume. Coalescence point is marked.

As initial and boundary conditions are not precisely known for the experiment, the agreement between experimental and numerical results seems reasonable. Moreover, the coalescence of two bubbles is equivalent to instantaneous film rupture in the BIM computation, while the liquid between the interfaces of two bubbles is gradually squeezed out in the experiment, so a slight difference is found in the expansion phase after the coalescence. Generally, the numerical results match the experimental observations well and the main features are well modelled in the BIM computation. Validity of the present model is thus proved.

Obviously, the moment when coalescence occurs is sensitive to the value of Δs. However, it remains unknown whether the value of Δs affects the main features of the coalesced bubble. The dependency of the numerical results on coalescence criterion Δs has also been investigated. Δs is selected as 0.02, 0.01 and 0.008 and bubble shapes at t = 2.22ms and t = 2.49ms are compared in Fig. 10. It can be seen that bubble shapes tend to coincide with the decrease of Δs. Considering the mesh size and the accuracy of the 3D numerical model, $\Delta s = 0.02$ is selected as the coalescence criterion in this paper.

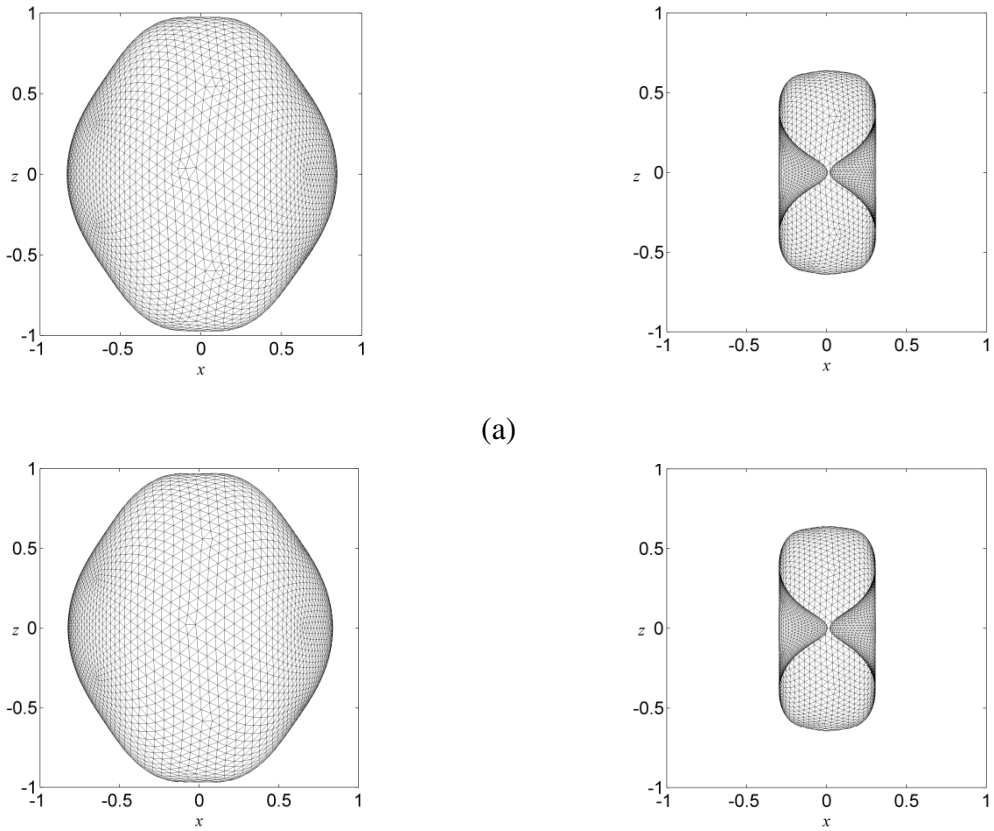

(a)

(b)

Fig. 10. Comparison of bubble shapes with different coalescence criterions (a) Δs=0.01 (b) Δs=0.008 at 2.22ms and 2.49ms, respectively.

6. Axisymmetric coalescence of two bubbles

Axisymmetric coalescence of two bubbles are considered, for which the centre line of two bubbles at inception is parallel to buoyancy (β = 0). Analyses are carried out in terms of the buoyancy parameter δ and the inter-bubble distance γ_{bb}.

6.1. Effects of buoyancy

Case 1: $\varepsilon = 50, R_0 = 0.1911, \delta = 0.1, \gamma_{bb} = 0.6$

In this case, the inter-bubble distance is $\gamma_{bb} = 0.6$, the buoyancy parameter is $\delta = 0.1$ and axisymmetric coalescence of two bubbles is illustrated in Fig. 11. Two bubbles are incepted simultaneously and expand rapidly. The liquid between two bubbles is gradually squeezed out and the film thinning is observed. As shown in Fig. 11(a), the coalescence criterion is satisfied while they are in the expansion phase, and the interfaces become flattened. Afterwards, the coalesced bubble continues to expand and the maximum volume is attained at t_* = 1.25. The expansion of the bottom is restrained by the weak buoyancy and the upward jet of the bubble bottom thus forms earlier than the downward jet of the top surface in the collapse phase. At t_* = 2.42, the two jets are about to collide with one another.

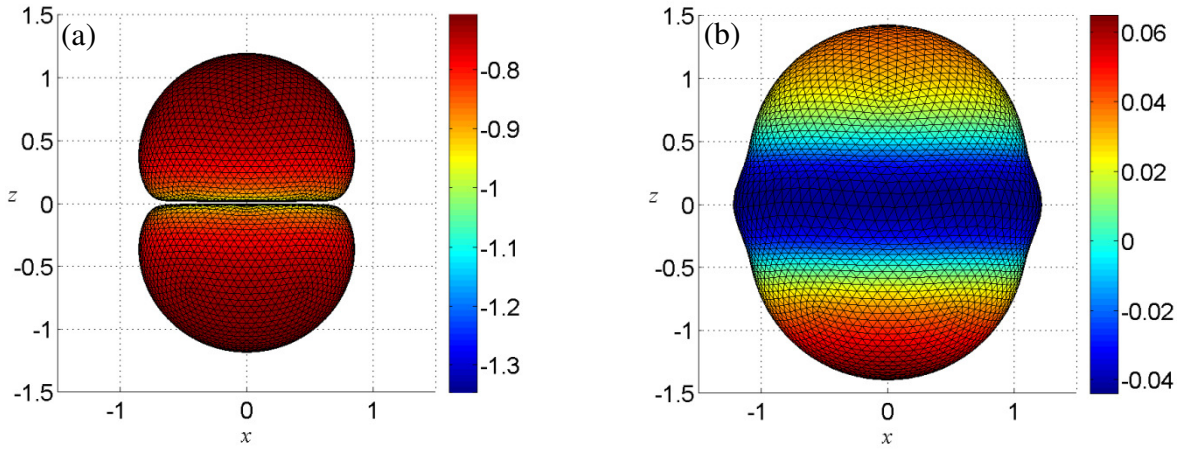

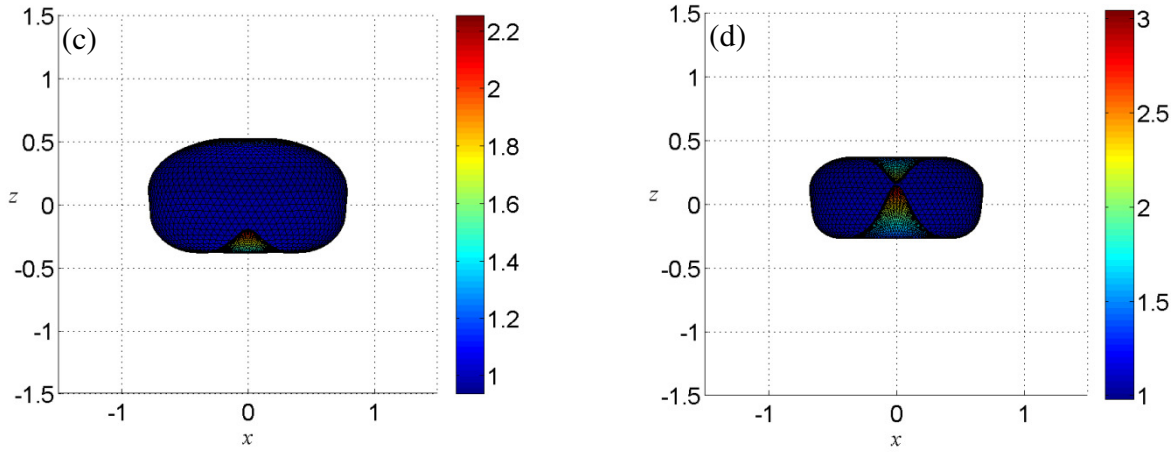

Fig. 11. Axisymmetric coalescence of two bubbles for $\varepsilon = 50, R_0 = 0.1911$, $\delta = 0.1$ and $\gamma_{bb} = 0.6$, during the dimensionless times t_*: (a) 0.42 (just before coalescence), (b) 1.25, (c) 2.35, and (d) 2.42, respectively.

After topology treatment for coalescence, there exists an annular indentation at the coalescence position. However, the subsequent evolution of the coalesced bubble results in a swelling of the bubble surface (see Fig. 11(b)). The velocity direction and magnitude and the amplified local view for the flow in the thin gap between the two bubbles are given in Fig. 12 to explain the phenomenon. In the expansion phase, the bubbles flatten and form a thin liquid film. The film thinning is driven by inertia of the liquid (Bremond et al., 2006). At the coalescence point, the flow in the thin gap between two bubbles moves radially outwards from the axis (see Fig. 12(b)), and the velocity magnitude of the flow around the 'stitch' line is the largest (see Fig. 12(a)). Therefore, the bubble surface at coalescence position gains a larger radial velocity, leading to the swelling in Fig. 11(b). Fig. 12 also suggests the fact that the ring in the experiment is caused by the radial flow.

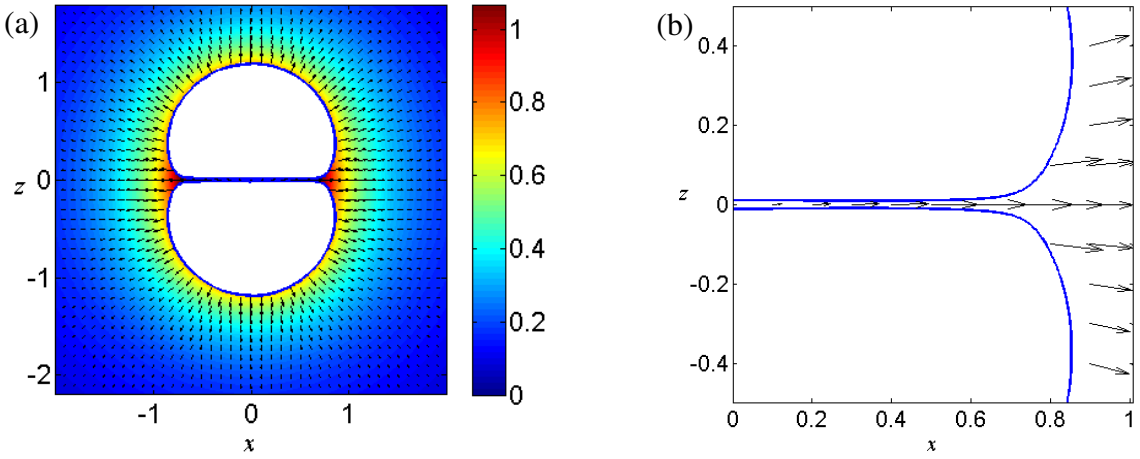

Fig. 12. (a) The velocity direction and magnitude for the case in Fig. 11, at the dimensionless time $t_* = 0.42$ (just before coalescence), and (b) the amplified local view for the flow in the thin gap between the two bubbles.

Case 2: $\varepsilon = 50, R_0 = 0.1911, \delta = 0.5, \gamma_{bb} = 0.6$

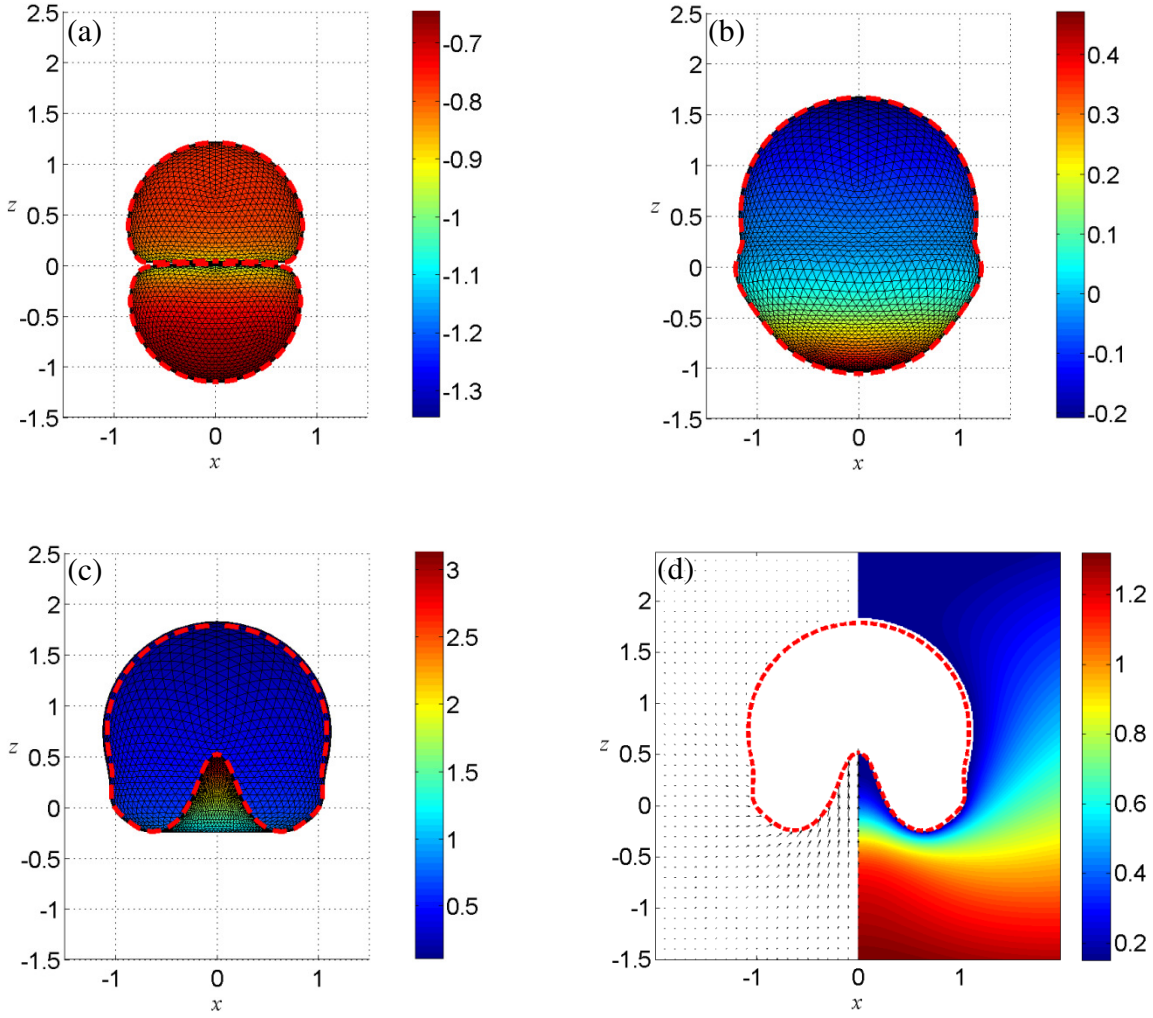

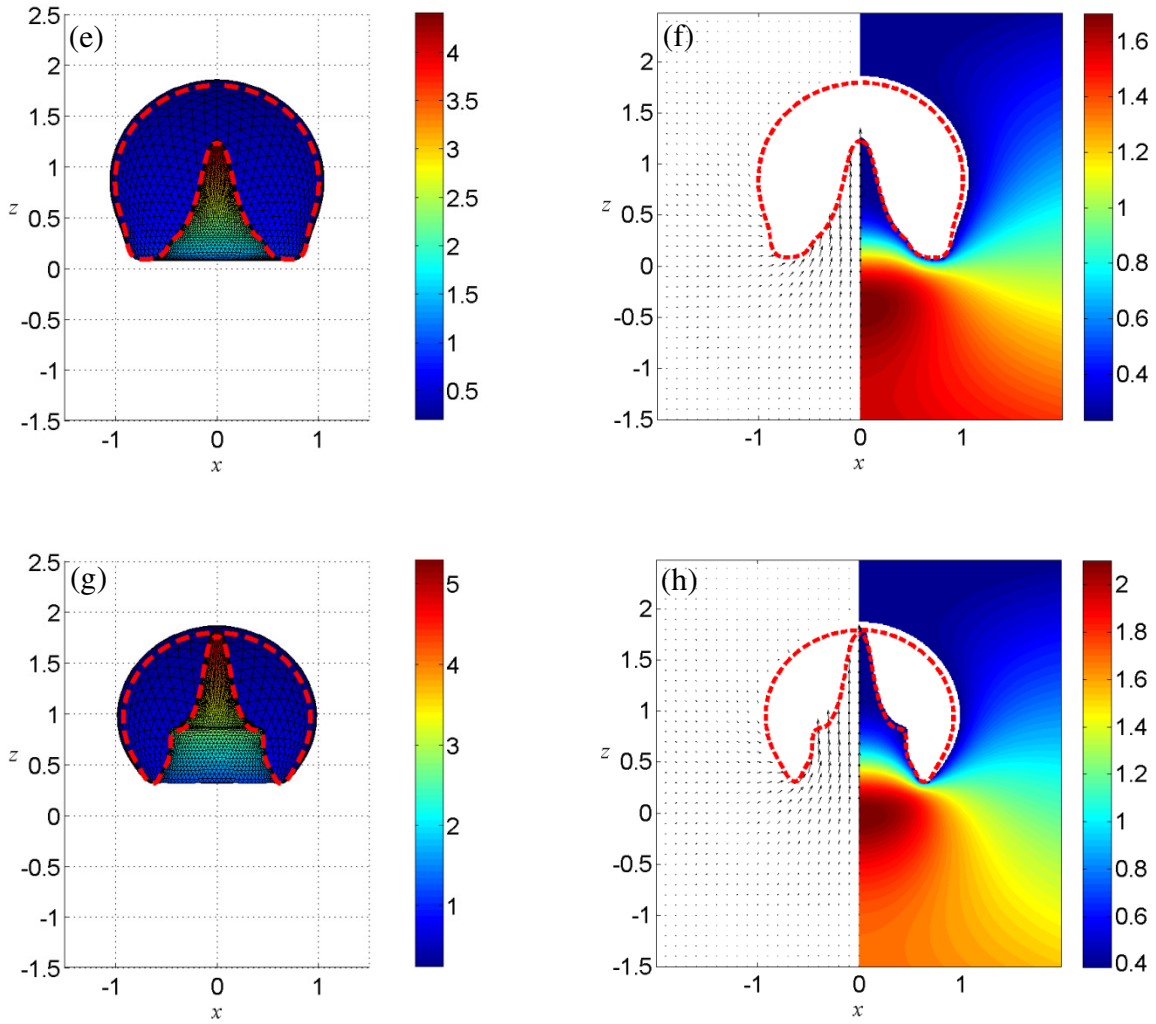

Fig. 13. Axisymmetric coalescence of two bubbles for $\varepsilon = 50, R_0 = 0.1911$, $\delta = 0.5$ and $\gamma_{bb} = 0.6$, during the dimensionless times t_*: (a) 0.45 (just before coalescence), (b) 1.32, (c,d) 2.00, (e,f) 2.25 and (g,h) 2.44, respectively, compared with the axisymmetric model (red dashed line).

In this case, the inter-bubble distance keeps $\gamma_{bb} = 0.6$, while the buoyancy parameter increases to $\delta = 0.5$. The buoyancy effect on the bubble is quite strong compared with case 1. Coalescence of two bubbles is illustrated in Fig. 13, compared with the axisymmetric model (red dashed line). Favourable comparison of bubble shape is observed. The small discrepancy between the two models is attributed to the difference in the mesh size. In the 3D simulation, a finer mesh is used for the jet surface to capture the jet evolution accurately, which leads to thinning out the element distribution in other regions. While in the axisymmetric simulation, nodes are evenly distributed over the bubble surface. The simulations also supply the evolution of the pressure and velocity in the liquid in the collapse phase of the coalesced bubble. See more details about the

calculations of the velocity and pressure fields in our previous paper (Li et al., 2016). At $t_* = 0.45$, the coalescence criterion is met and they are still expanding. The two coalescence surfaces arch up slightly. Afterwards, the coalesced bubble continues to expand. When the bubble attains the maximum volume at $t_* = 1.32$, the expansion of the bottom is restrained by the strong buoyancy. In the collapse phase, only an upward jet is observed. Fig. 13(d, f, h) shows the pressure and velocity fields after the upward jet formation. The velocity field is shown in the left half, and the pressure field is shown in the right half. From the velocity and pressure fields at $t_* = 2.00$, it can be seen that the jet formation is induced by the pressure gradient in the flow field. As the jet evolves, the fluid is drawn rapidly into the jet zone and a high-pressure region is gradually formed below the coalesced bubble. Jet formation is now sustained by the high pressure building up below the coalesced bubble (see Fig. 13(e)). Just prior to the jet impact at $t_* = 2.44$, the computation is stopped. An upward migration of the high-pressure region is observed and a crown-like skirt surrounding the liquid jet is formed.

What calls for special attention is the crown-like skirt at the base of the jet observed in Fig. 13(e). It's reckoned that this phenomenon is similar to the re-entrant jet in the work by Zhang et al. (2013). The crown-like skirt is actually the secondary jet of the coalesced bubble, which is related to the high-pressure region below the bubble (see Fig. 13(f)). The high-pressure region drives the advancing of the upward jet and also induces a wider secondary jet at the base of the upward jet.

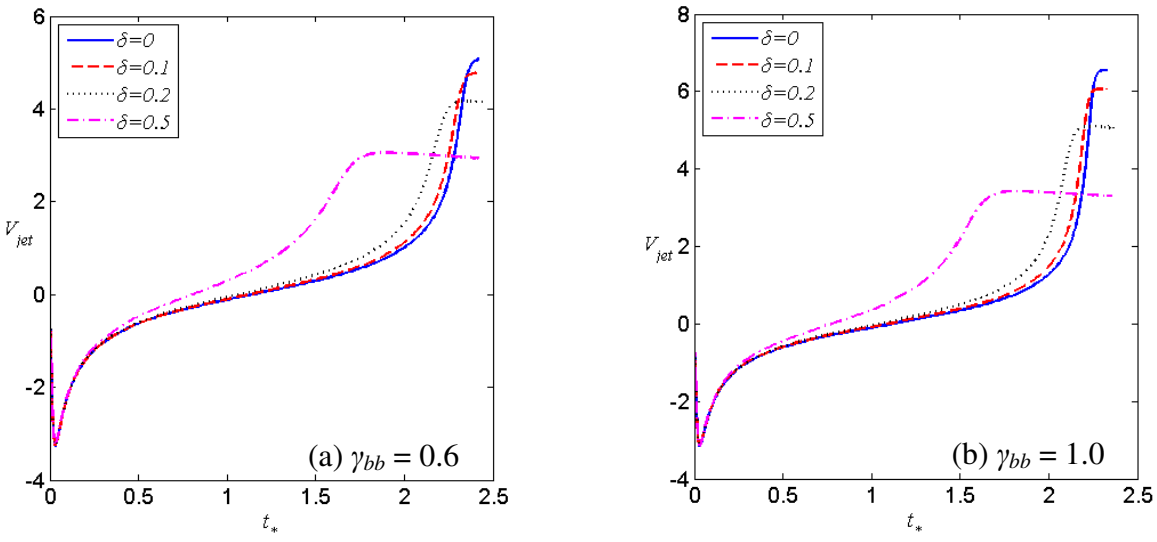

Fig. 14. Effects of buoyancy parameter on velocity of the upward jet with (a) $\gamma_{bb} = 0.6$ and (b) $\gamma_{bb} = 1.0$. The parameters used are $\varepsilon = 50, R_0 = 0.1911$.

Without considering the buoyancy effect, two jets shooting towards each other are formed

and contact in the middle of the coalesced bubble (see Fig. 7 and Fig. 8). If the effect of the buoyancy is considered, as the two cases given above, the bottom surface forms jet earlier while the top surface forms jet later. Therefore, the contact point of the two jets migrates upward with increasing buoyancy parameter δ. If the buoyancy parameter increases to a certain value, only an upward jet is observed. Effects of buoyancy parameter δ on velocity history of the upward jet are investigated. With γ_{bb} = 0.6 and γ_{bb} = 1.0, the histories of the upward jet velocity for various buoyancy parameters δ are illustrated in Fig. 14. The varying pattern of the jet velocity history with γ_{bb} = 0.6 is the same as that with γ_{bb} = 1.0. The increase of the buoyancy parameter δ makes the jet velocity at the impact decrease, but has little effect on the jet impact moment.

6.2. Effects of inter-bubble distance

Case 3: $\varepsilon = 50, R_0 = 0.1911, \delta = 0.5, \gamma_{bb} = 1.0$

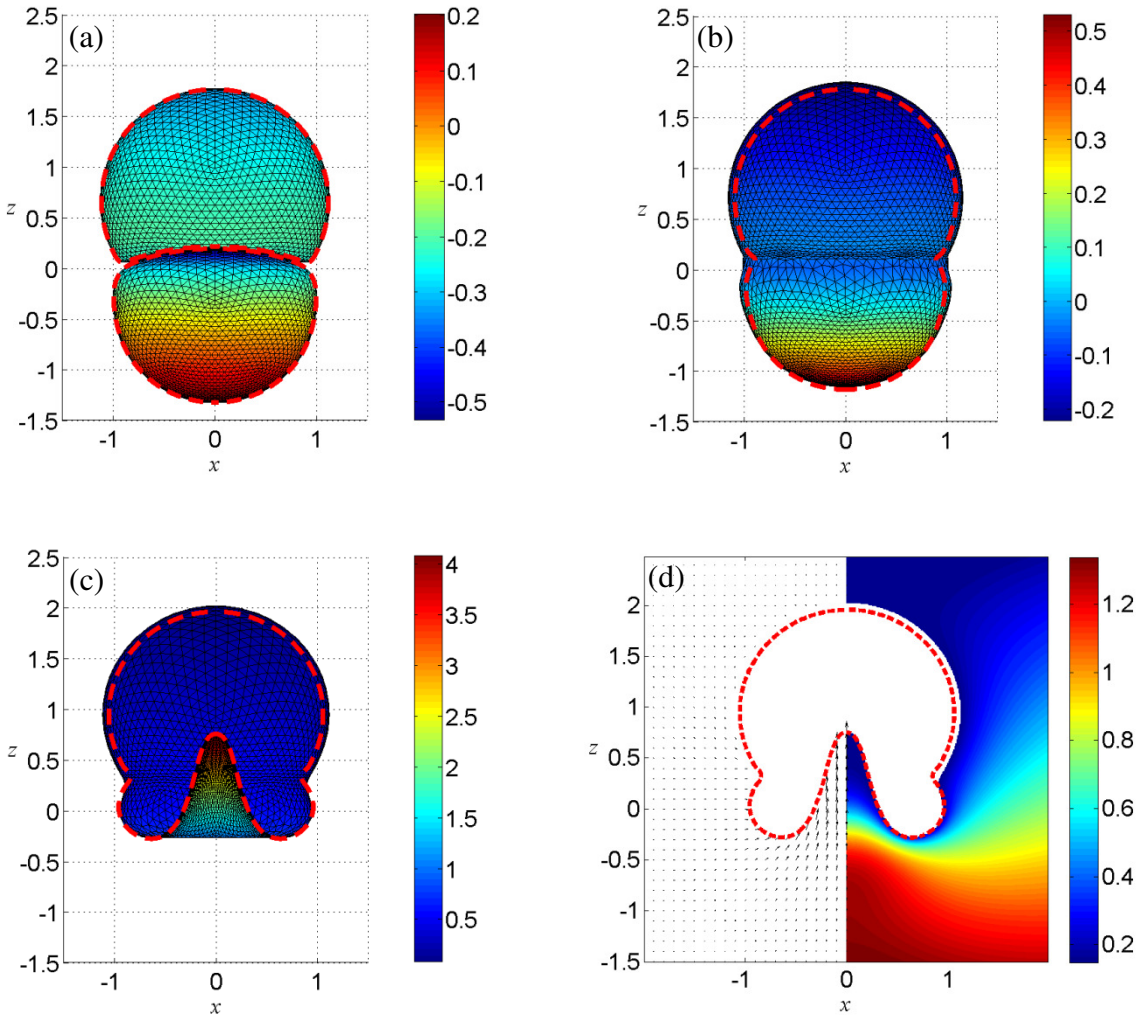

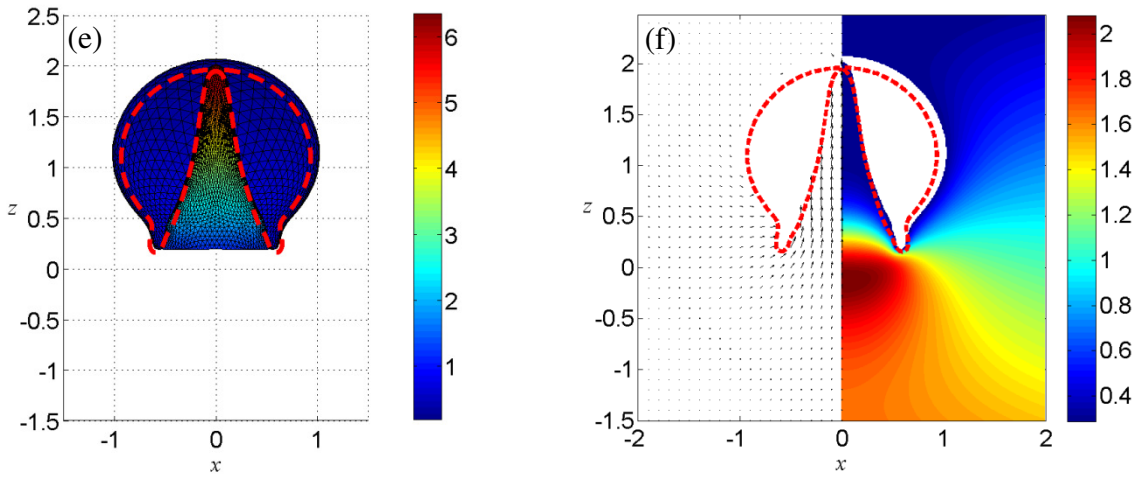

Fig. 15. Axisymmetric coalescence of two bubbles for $\varepsilon = 50, R_0 = 0.1911$, $\delta = 0.5$ and $\gamma_{bb} = 1.0$, during the dimensionless times t_*: (a) 1.10 (just before coalescence), (b) 1.30, (c,d) 2.00 and (e,f) 2.38, respectively, compared with the axisymmetric model (red dashed line).

In this case, the inter-bubble distance is $\gamma_{bb} = 1.0$ and the buoyancy parameter is $\delta = 0.5$. Coalescence of two bubbles is illustrated in Fig. 15, compared with the axisymmetric model (red dashed line). Favourable comparison of bubble shape is observed. Compared with case 2, the increase of the inter-bubble distance delays the coalescence of two bubbles. The bubble shapes just before coalescence at t_* = 1.10 are shown in Fig. 15(a) and an obvious upward migration of the two bubbles is observed due to the strong buoyancy. The maximum volume of the coalesced bubble is attained at t_* = 1.30 and an annular indentation at the coalescence point still exists at the moment. In the collapse phase, an upward jet is formed due to the effect of the buoyancy (see Fig. 15(c)). At the jet impact, a high-pressure region is formed below the coalesced bubble (similar to that in case 2). However, the early occurrence of the jet impact in this case makes it impossible to observe the crown-like skirt in case 2.

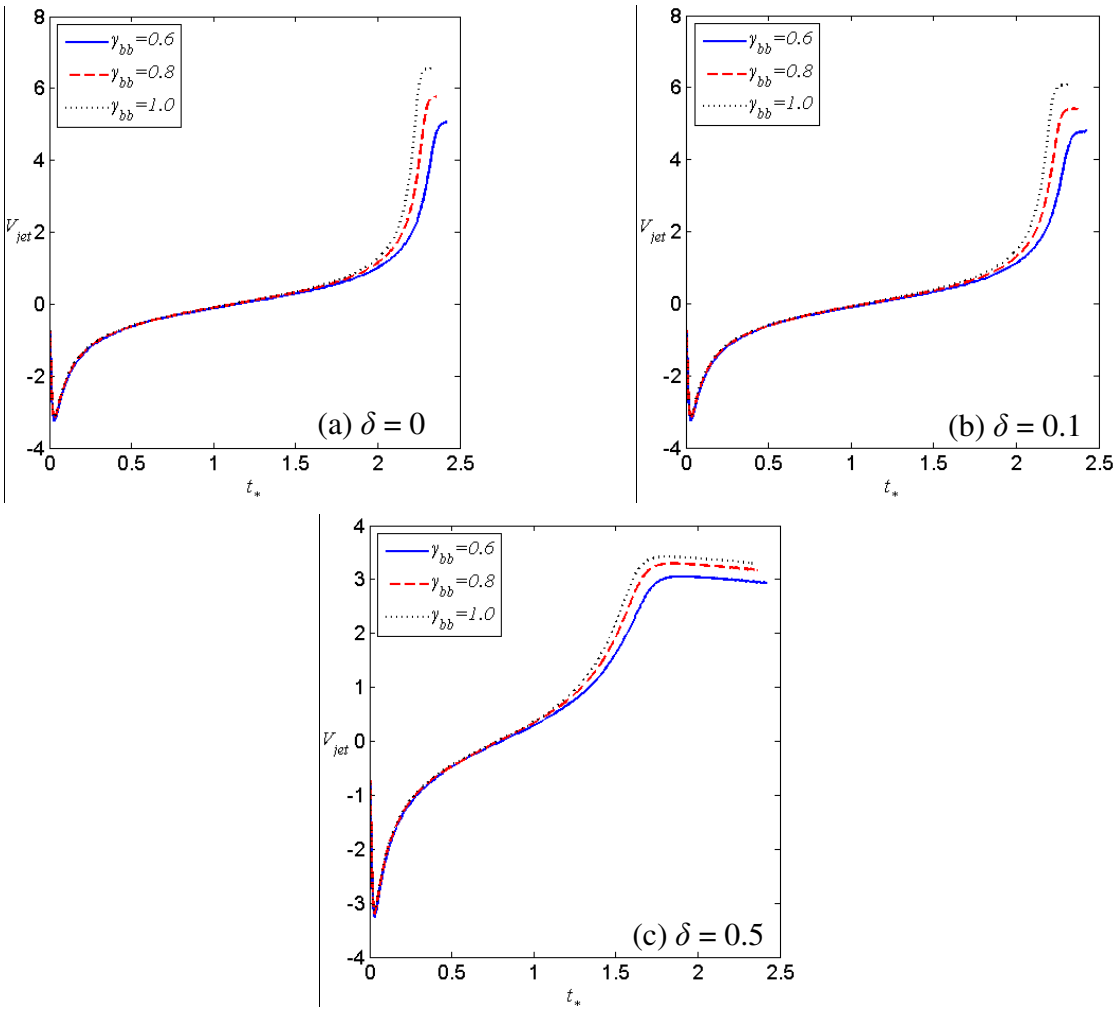

Fig. 16. Effects of inter-bubble distance on jet velocity with (a) $\delta = 0$, (b) $\delta = 0.1$ and (c) $\delta = 0.5$. The parameters used are $\varepsilon = 50, R_0 = 0.1911$.

Effects of inter-bubble distance γ_{bb} on velocity variation of the upward jet are investigated. With δ = 0, δ = 0.1 and δ = 0.5, the time histories of the upward jet velocity for various inter-bubble distances γ_{bb} are illustrated in Fig. 16. The same varying pattern of the jet velocity is obtained. In fact, the increase of γ_{bb} represents weak mutual interactions. If the buoyancy parameter δ is fixed, the increase of γ_{bb} leads to earlier contraction of the coalesced bubble and earlier occurrence of jet impact. It's found that the jet velocity at the impact increases with γ_{bb}.

7. 3D coalescence of two bubbles in a horizontal configuration

In this section, we perform the numerical studies of the coalescence of two bubbles in a horizontal configuration, where the angle between the centre line and the direction of buoyancy is $\beta = \pi/2$. The effects of the buoyancy parameter δ and the inter-bubble distance γ_{bb} are investigated. Calculations also provide information on the velocity and pressure fields surrounding the bubbles.

Meanwhile, time histories of the total bubble volume, centroid motion and Kelvin impulse are also illustrated.

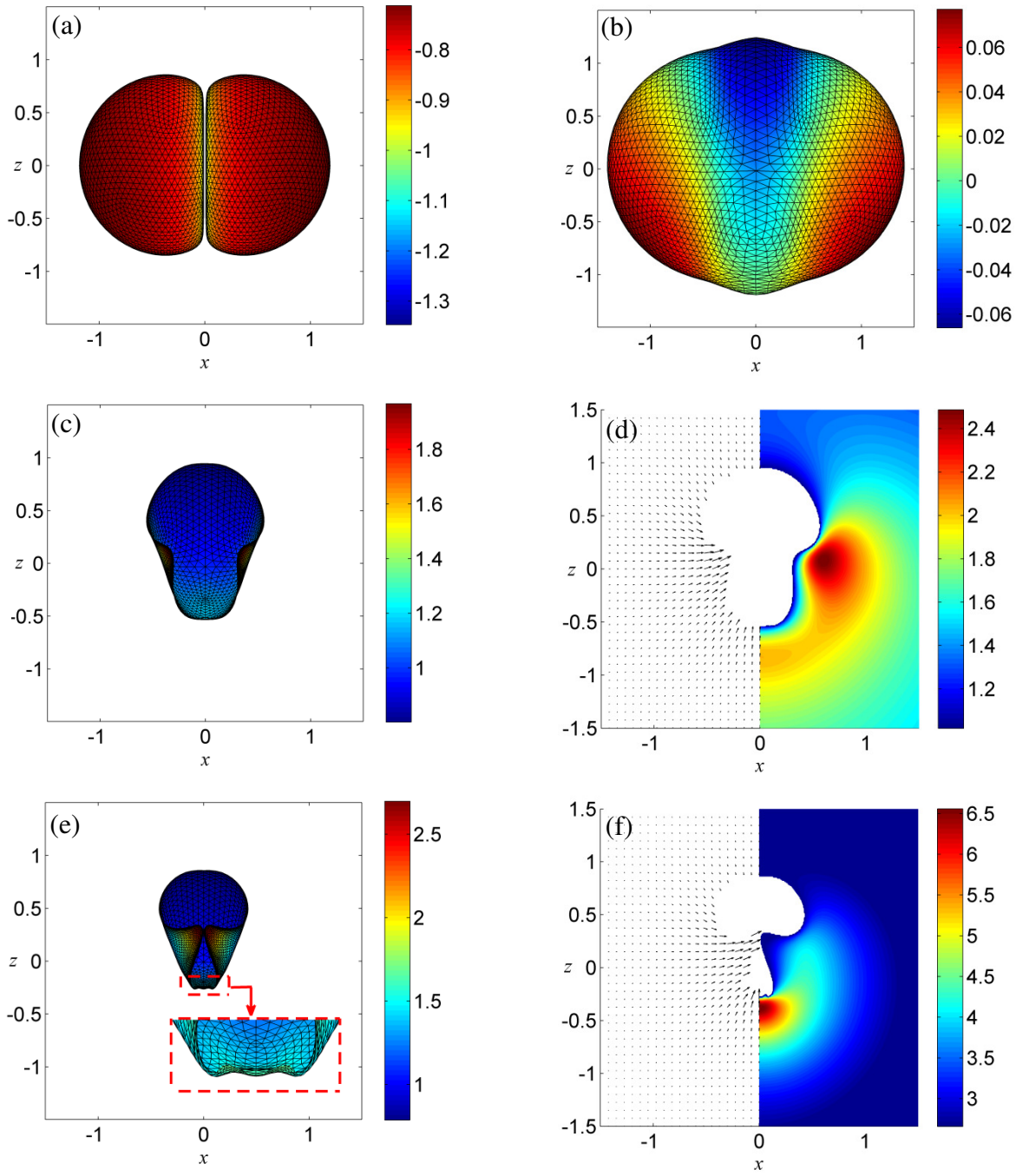

Fig. 17. 3D coalescence of two bubbles in a horizontal configuration for $\gamma_{bb} = 0.6$, $\delta = 0.2$. The corresponding time is (a) $t_* = 0.44$ (just before coalescence), (b) $t_* = 1.26$, (c,d) $t_* = 2.36$ and (e,f) $t_* = 2.44$. In the computation, the parameters used are $\varepsilon = 50, R_0 = 0.1911$.

In the first case, the inter-bubble distance is $\gamma_{bb} = 0.6$ and the buoyancy parameter is $\delta = 0.2$.

The bubble shapes at typical times are shown in Fig. 17. At $t_* = 0.44$ just before coalescence, the buoyancy has little effect on the bubble shapes. After coalescence, a swelling near the coalescence position is observed at $t_* = 1.26$ when the maximum volume is attained. As mentioned above, the elongated ends along the center line should collapse faster and form horizontally directed jet. In the presence of the buoyancy, however, the parts that collapse faster move downward along the coalesced bubble surface. In Fig. 17 (c), two jets are formed and directed towards each other with a small vertical deviation. The collapse draws the fluid into the jet zone rapidly, and the increased fluid mobility near the jet leads to the formation of high-pressure region. In Fig. 17 (d), there exist three high-pressure regions at $t_* = 2.36$, two near the two jet zones and one below the coalesced bubble. The high-pressure regions near jet zones drive the two jets and the pressure peaks are the highest in the flow field. At $t_* = 2.44$ just before the collision of the two jets, an indentation on the bottom surface is observed (see Fig. 17 (e)). The pressure around the jet zones and below the bottom increases. At this moment, the pressure peak of the high-pressure region below the bubble is the highest in the flow field. It can be predicted that the upward jet will be sustained by the high pressure building up below the bubble.

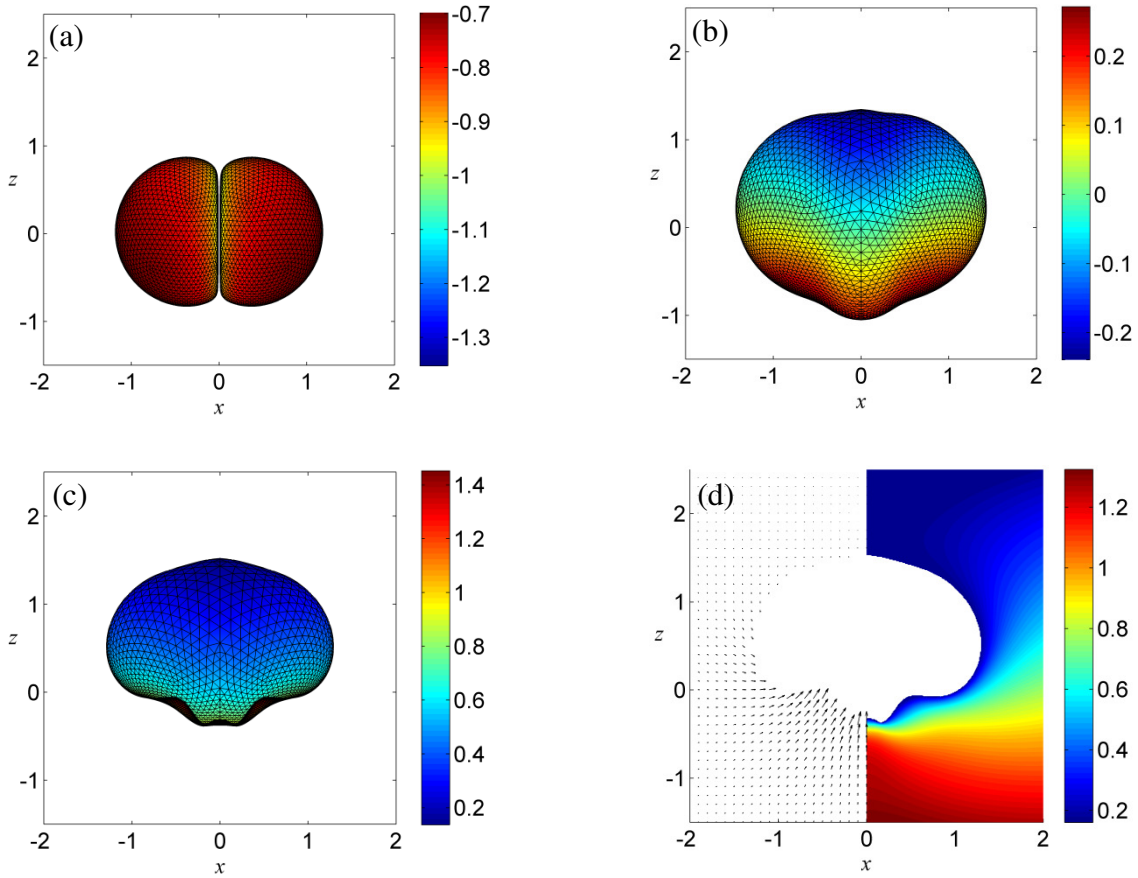

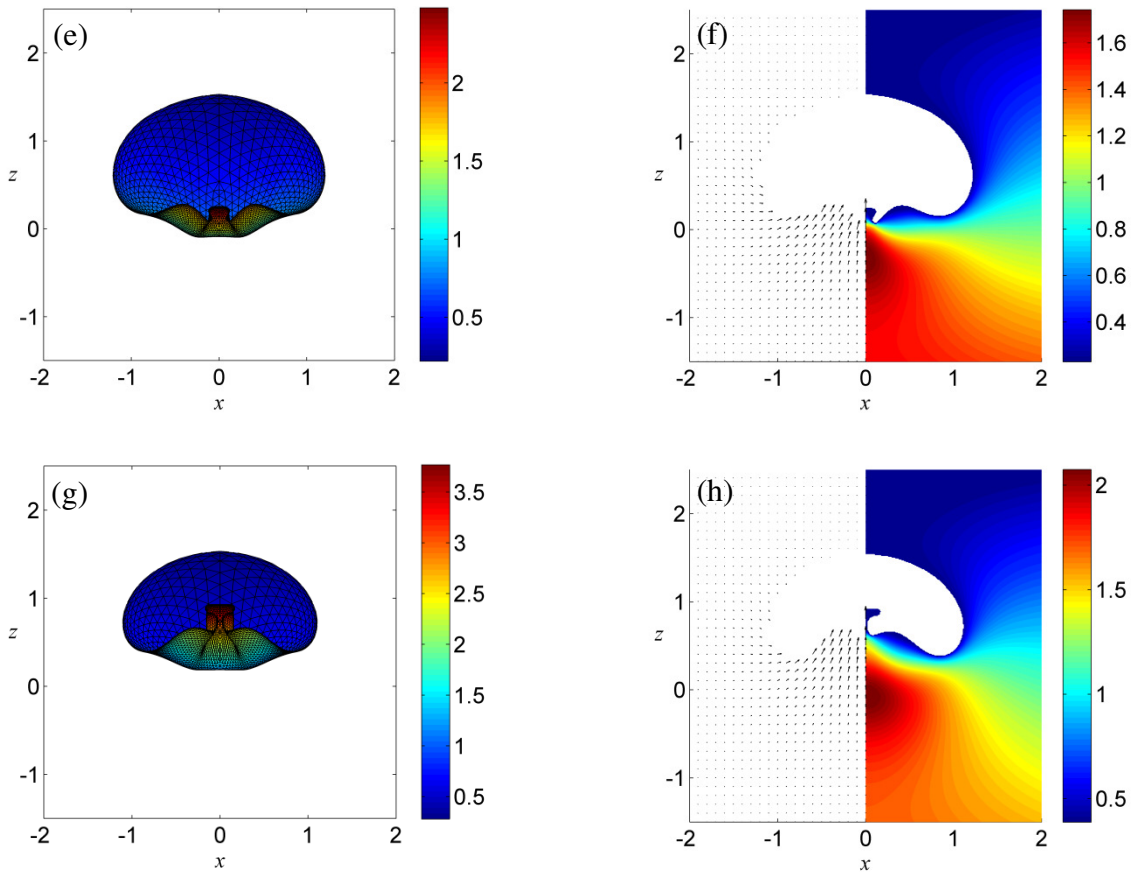

Fig. 18. 3D coalescence of two bubbles in a horizontal configuration for $\gamma_{bb} = 0.6$, $\delta = 0.5$. The corresponding time is (a) $t_* = 0.44$ (just before coalescence), (b) $t_* = 1.29$, (c,d) $t_* = 1.97$ (e,f) $t_* = 2.04$ and (g,h) $t_* = 2.36$. In the computation, the parameters used are $\varepsilon = 50, R_0 = 0.1911$.

If $\gamma_{bb} = 0.6$ and $\delta = 0.5$, the features of the coalescence change a lot. The bubble shapes at typical times are illustrated in Fig. 18, and the velocity and pressure fields are also given. The computation is stopped at $t_* = 2.36$. Bubble shapes just before coalescence are similar to those in Fig. 17(a). After coalescence, the joined bubble attains the maximum volume at $t_* = 1.29$. From the above discussions, it's noted that the presence of buoyancy affects the locations where jets originate. Affected by the strong buoyancy in this case, the locations where two jets originate approach to the bubble bottom. In the collapse phase, two jets are formed and the bubble bottom contracts rapidly due to the pressure gradient. At $t_* = 1.97$, two jets are directed towards each other with large vertical deviation, and an upward jet with a flattened tip originates on the bubble bottom. As shown in Fig. 18(d), the pressure gradient below the coalesced bubble is obvious, leading to the upward jet formation. As the upward jet evolves, a high-pressure region is thus gradually formed below the coalesced bubble (see Fig. 18(f)). Meanwhile, the directions of another two jets are affected by the buoyancy. Afterwards, the high-pressure region drives the

advancing of the upward jet. At t_* = 2.36, a larger high-pressure region is observed and the pressure peak increases. In this case, there is no high-pressure region formed near the oblique jet zone in the whole process.

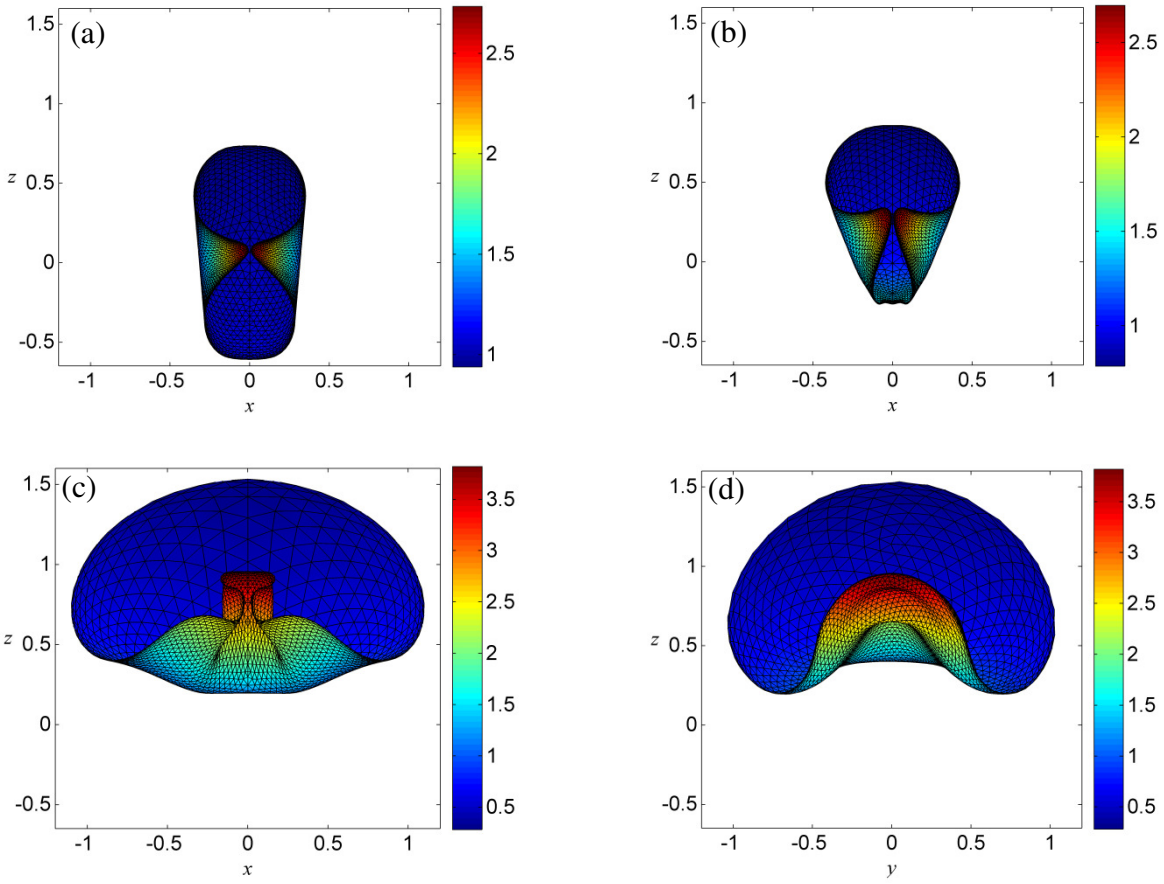

Fig. 19. Front view of the jet formation in the coalescence of two bubbles in a horizontal configuration with different buoyancy parameters (a) δ = 0.1 (b) δ = 0.2 and (c) δ = 0.5 when γ_{bb} = 0.6. Side view of the jet formation with δ = 0.5 is shown in (d). In the computation, the parameters used are ε = 50, R_0 = 0.1911. The corresponding time is (a) t_* = 2.42 (b) t_* = 2.44 and (c,d) t_* = 2.36.

When γ_{bb} = 0.6, the bubble shapes at the jet impact for various buoyancy parameters δ are illustrated in Fig. 19. It's known that two jets along the centre line are formed after coalescence in zero-buoyancy cases (see Fig. 7 and Fig. 8). When δ = 0.1, the locations where the two jets originate move a little downward and the two jets are directed horizontally with a small vertical deviation due to the weak buoyancy. If the buoyancy parameter δ increases, the locations where the two jets originate move downward and approach to the bottom surface. With increasing δ, the larger vertical deviation of the two jets and later occurrence of jet impact are noted. If the

buoyancy parameter increases to δ = 0.5, the two oblique jets and an upward jet are observed. Front view and side view of the jet formation at t_* = 2.36 are shown in Fig. 19(c) and Fig. 19(d). We note the flattened tip of the upward jet. The middle of the upward jet is crushed by another two jets and an arc bulge is thus observed in Fig. 19(d). It's reckoned that the three jets are merged into one upward jet and that it will finally penetrate the coalesced bubble.

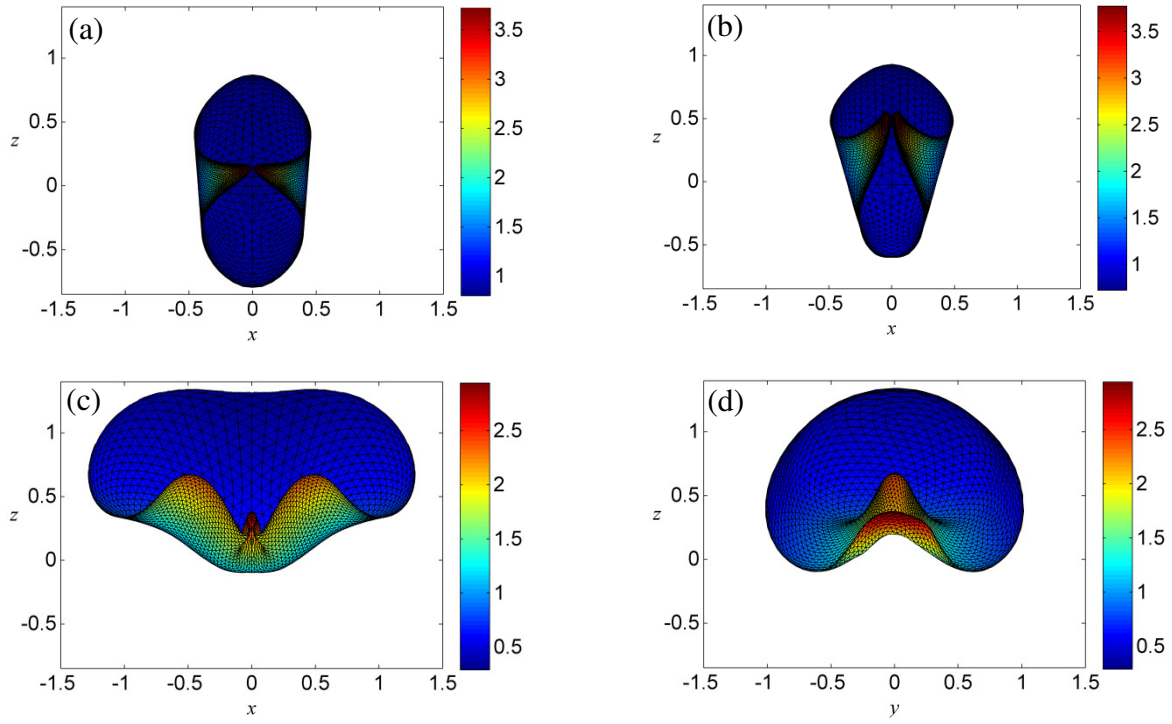

Fig. 20. Front view of the jet formation in the coalescence of two bubbles in a horizontal configuration with different buoyancy parameters (a) δ = 0.1 (b) δ = 0.2 and (c) δ = 0.5 when γ_{bb} = 1.0. Side view of the jet formation with δ = 0.5 is shown in (d). In the computation, the parameters used are ε = 50, R_0 = 0.1911. The corresponding time is (a) t_* = 2.33 (b) t_* = 2.37 and (c) t_* = 2.24.

When γ_{bb} = 1.0, the bubble shapes at the jet impact for various buoyancy parameters δ are illustrated in Fig. 20. Comparing the bubble shapes to those in Fig. 19, it's found that the vertical deviation of the two jets becomes larger with increasing γ_{bb}. For δ = 0.1 and δ = 0.2, the jet impact occurs earlier when γ_{bb} = 1.0. For δ = 0.5, as shown in Fig. 20(c) and Fig. 20(d), two jets are almost vertically directed. Besides, a thin upward jet originates on the bubble bottom.

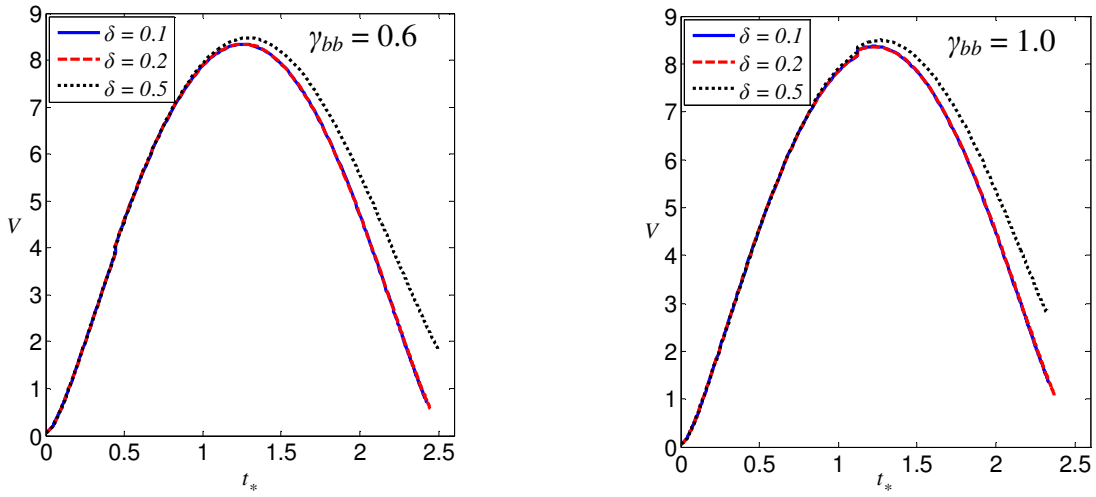

(a)

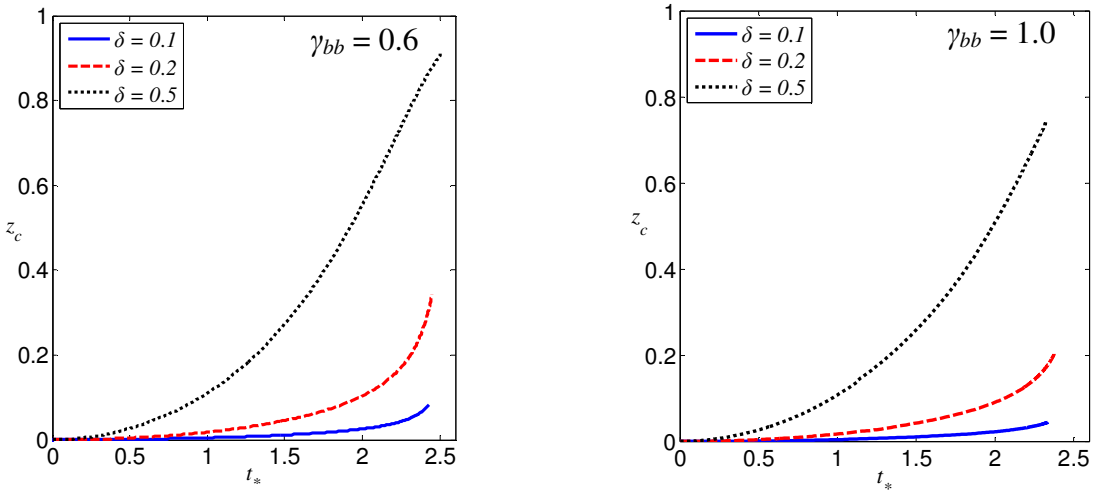

(b)

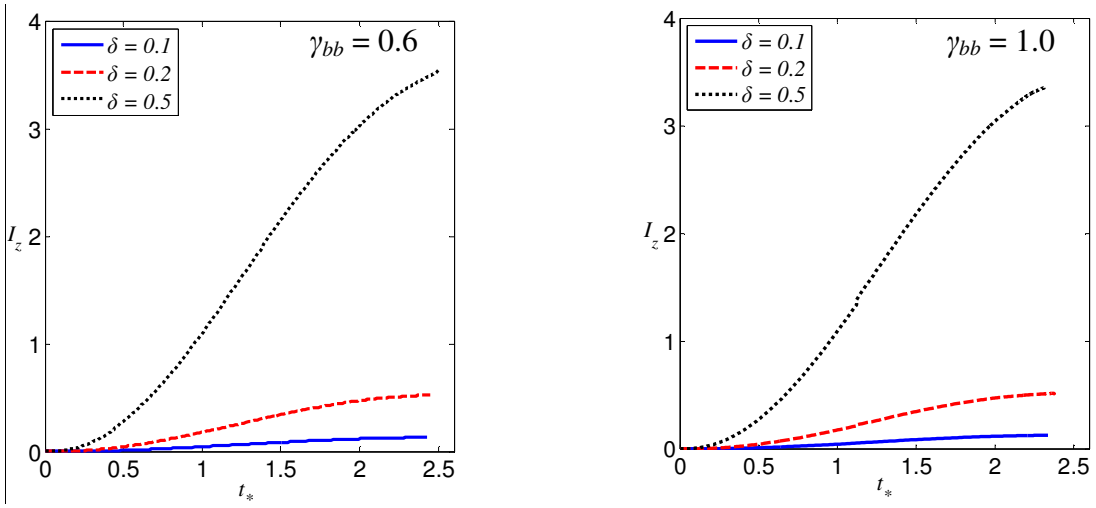

(c)

Fig. 21. Effects of buoyancy parameter δ on time histories of (a) the total bubble volume, (b) centroid motion of the bubble system along the z-axis and (c) z-component of Kelvin impulse for

the bubble system.

For the two-bubble system in this section, the effects of δ on the total bubble volume, centroid motion of the bubble system along the z-axis and z-component of Kelvin impulse for the system are given in Fig. 21. From Fig. 21(a), it's found that the buoyancy parameter δ has little effect on the coalescence point; the key factor is the inter-bubble distance γ_{bb}. Histories of the total volume in the expansion phase for different δ nearly coincide. With increasing δ, however, the maximum volume attained in the coalescence becomes larger, and a slower contraction is also noted. Similar results are also obtained in the axisymmetric configuration (not shown in this paper). Centroid motion of the two bubbles along the z-axis is shown in Fig. 21(b). The centroid of the bubble system keeps migrating upward due to buoyancy. The upward velocity of the centroid increases in the whole process and a rapid rise in the upward velocity is observed towards the end of the collapse phase. It's clear that the increase of δ leads to a faster and larger upward migration of the bubble system. Time histories of the z-component of Kelvin impulse for different buoyancy parameters are compared in Fig. 21(c). The whole system achieves a Kelvin impulse due to the buoyancy force which is related to the buoyancy parameter and bubble volume. The Kelvin impulse can be regarded as linear momentum of 'the bubble' if a virtual mass induced by the fluid motion is attributed to the cavity (Vogel et al., 1989). Therefore, the z-component of the Kelvin impulse rises rapidly in the expansion phase. However, the buoyancy force reduces in the collapse phase, leading to the slow increase of the Kelvin impulse. Since the induced virtual mass reduces during the bubble collapse and the Kelvin impulse increases slowly, the translational velocity of the bubble centre has to increase rapidly (see Fig. 21(b)). From the above discussions, it's clear that the z-component of the Kelvin impulse increases faster with the increase of the buoyancy parameter δ.

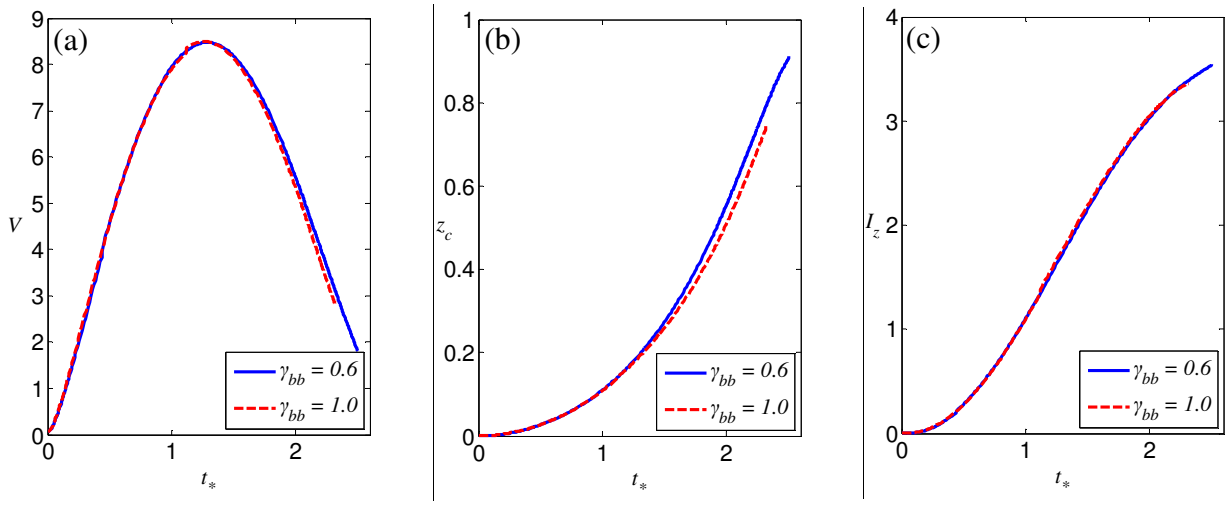

Fig. 22. Effects of inter-bubble distance γ_{bb} on time histories of (a) the total bubble volume, (b) centroid motion of the bubble system along the z-axis and (c) z-component of Kelvin impulse for the bubble system. The buoyancy parameter is $\delta = 0.5$.

When δ = 0.5, time histories of some quantities for different inter-bubble distances are compared in Fig. 22. As shown in Fig. 22(a), the inter-bubble distance γ_{bb} has little effect on the bubble volume in the expansion phase. If γ_{bb} increases, the bubble volume decreases faster in the collapse phase, that is to say the increasing γ_{bb} leads to an earlier jet impact of the coalesced bubble. As shown in Fig. 22(b), the upward velocity of the centroid decreases with γ_{bb}. Fig. 22(c) suggests that the effect of the inter-bubble distance γ_{bb} on the Kelvin impulse can be neglected. In conclusion, the buoyancy parameter δ plays an important role in dynamic behaviours in the coalescence of two bubbles while the inter-bubble distance γ_{bb} affects the jet impact moment.

8. 3D coalescence of two bubbles in an oblique configuration

In this section, we perform the numerical studies of the coalescence of two bubbles in an oblique configuration. The angle between the centre line and the direction of buoyancy is $\beta = \pi/4$, which means two bubbles are symmetric with respect to the plane $z = -x$. We explore the effects of the buoyancy parameter δ on dynamic behaviours in this part. The inter-bubble distance is γ_{bb} = 0.6, bubble shapes in the 3D coalescence for δ = 0.1, 0.2 and 0.5 are given. Calculations also provide information on the pressure field surrounding the bubbles. Meanwhile, time histories of the total bubble volume, centroid motion and Kelvin impulse are compared.

3D coalescence of two bubbles in an oblique configuration for γ_{bb} = 0.6 and δ = 0.1 is shown in Fig. 23. Bubble shapes at five typical times are illustrated in Fig. 23(a). In the first and second frames, the weak buoyancy has little effect on the bubble shapes in the expansion phase. The

coalescence criterion is met at $t_* = 0.44$ and the maximum volume of the coalesced bubble is attained at $t_* = 1.26$. The elongated ends of the bubble with higher curvature are marked with A and B (second frame) and collapse first (Vogel et al., 1989). The surrounding fluid is thus drawn rapidly (see the third frame). The lower part marked with B collapse faster than the upper part due to the buoyancy. At $t_* = 2.33$, a jet directed diagonally towards the upper bubble is observed. Then a jet directed diagonally towards the lower bubble is formed. At $t_* = 2.42$, the two jets are about to contact. In this process, a slight upward migration is observed due to the weak buoyancy. Pressure fields at the last two moments are also given in Fig. 23(b). As the collapse proceeds, two high-pressure regions are produced around the parts that collapse faster. In the first frame, the pressure peak of the lower high-pressure region is the highest in the flow field. The two high-pressure regions drive the advancing of the two jets. At the jet impact, there still exist two high-pressure regions with higher pressure peaks. Now the pressure peak of the upper high-pressure region is the highest in the flow field. The axis connecting initial bubble centres is also plotted in the second frame. The jet directed diagonally towards the upper bubble has a slight vertical deviation due to the weak buoyancy.

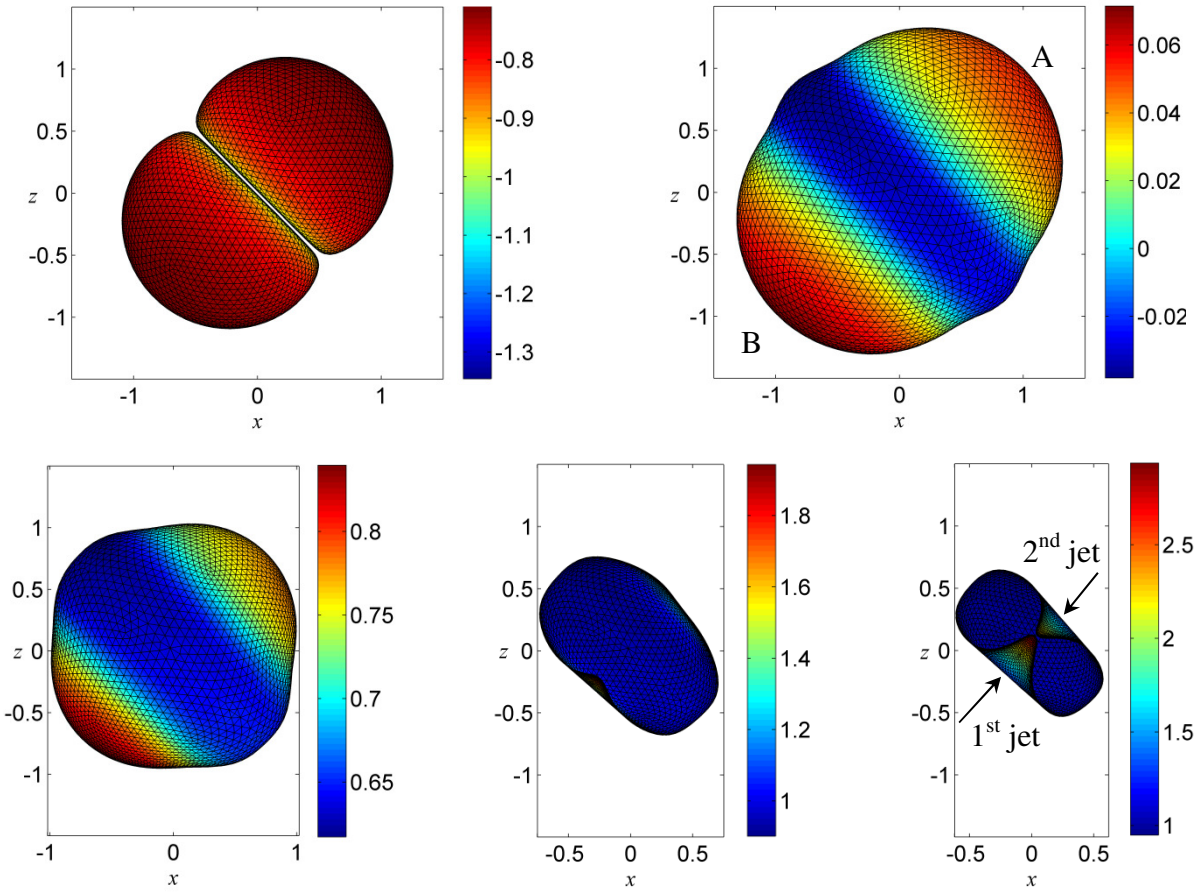

(a)

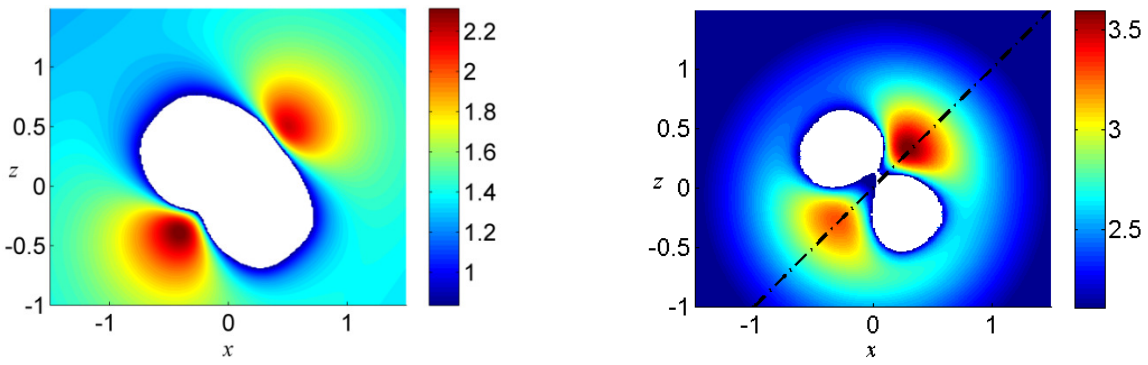

(b)

Fig. 23. 3D coalescence of two bubbles in an oblique configuration for $\gamma_{bb} = 0.6$ and $\delta = 0.1$. (a) Evolution of bubble shapes at $t_* = 0.44$, 1.26, 2.00, 2.33 and 2.42. (b) Pressure fields at $t_* = 2.33$ and 2.42, with the axis connecting initial bubble centres plotted. In the computation, the parameters used are $\varepsilon = 50, R_0 = 0.1911$.

3D coalescence of two bubbles in an oblique configuration for $\gamma_{bb} = 0.6$ and $\delta = 0.2$ is shown in Fig. 24. Bubble shapes at five typical times are illustrated in Fig. 24(a). Coalescence of two bubble occurs at $t_* = 0.45$, and the maximum volume of the coalesced bubble is attained at $t_* = 1.25$. In the second frame, the parts marked with A and B should have collapsed first in the collapse phase, however, the presence of buoyancy makes the positions where jets originate move downward along the bubble surface (marked with A′ and B′ in the third and fourth frames, respectively). In the third frame, the lower part B′ contracts faster due to the buoyancy. A jet directed diagonally towards the upper bubble forms earlier, but with a vertical deviation. At $t_* = 2.46$, another jet that originates on the bubble surface A′ is observed and the two jets are about to collide. In this process, the upward migration of the coalesced bubble is larger than that in the last case. The main interest in this case is a third jet forming at the bubble bottom (shown in the last frame). Evolution of pressure field after jet formation is given in Fig. 24(b). In the first frame, the increased fluid mobility near B′ produces a high-pressure region that induces jet formation and sustains the advancing of the 1st jet. At this moment, there also exists a high-pressure region near the right side of the coalesced bubble, and the pressure peak is about 1.35. The high-pressure region induces the formation of the 2nd jet. Afterwards, the pressure peaks of the two high-pressure regions keep increasing, as shown in the second and third frames. Meanwhile the lower high-pressure region moves gradually towards the bubble bottom. At $t_* = 2.46$, two high-pressure regions with higher pressure peaks are observed. Now the lower high-pressure region is below the bubble bottom, which leads to the formation of the 3rd jet. The axis

connecting initial bubble centres is also plotted in the last frame. Obviously, a large upward migration of the coalesced bubble is observed. Besides, the 1st jet directed diagonally towards the upper bubble has an obvious vertical deviation due to the buoyancy.

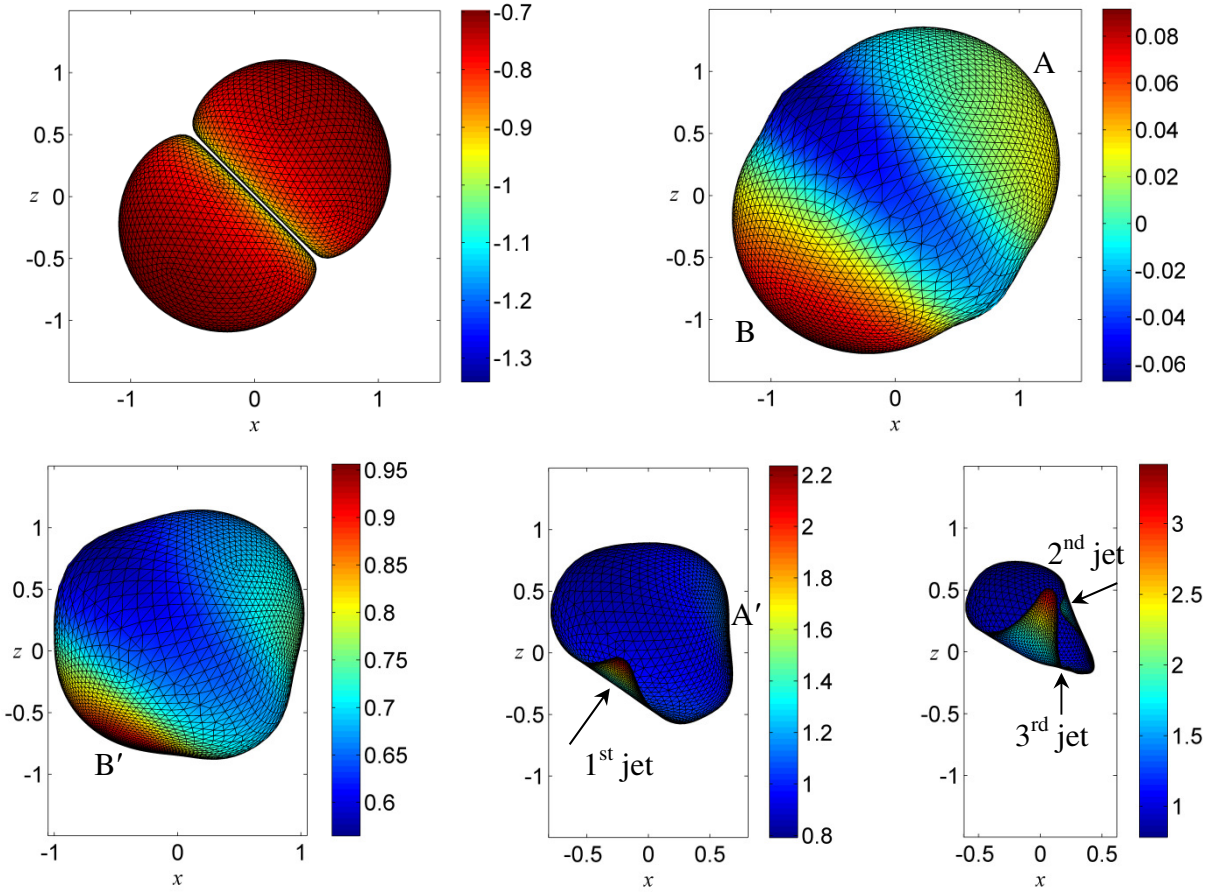

(a)

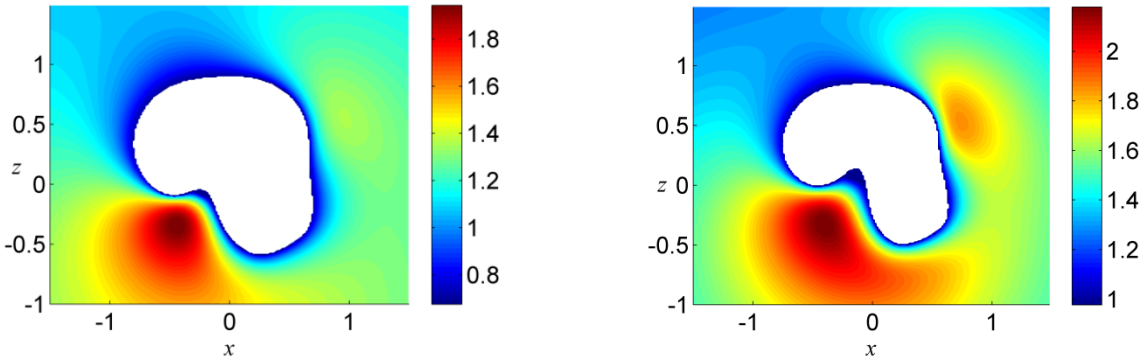

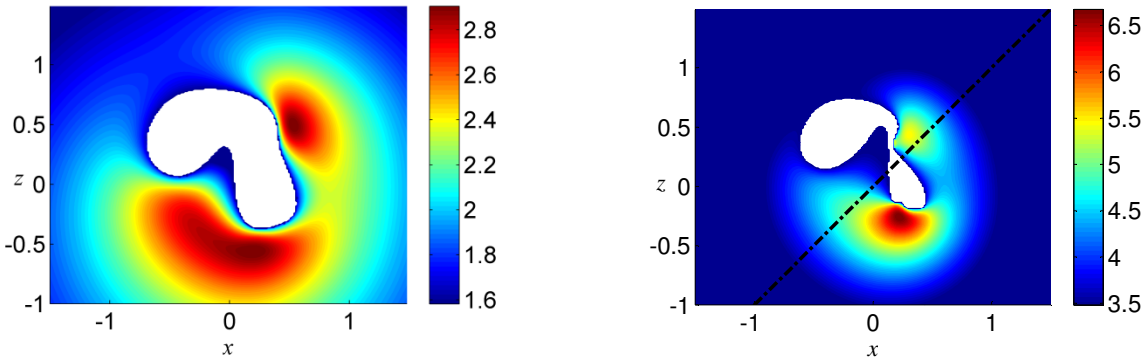

(b)

Fig. 24. 3D coalescence of two bubbles in an oblique configuration for γ_{bb} = 0.6 and δ = 0.2. (a) Evolution of bubble shapes at t_* = 0.45, 1.25, 2.00, 2.30 and 2.46. (b) Pressure fields at t_* = 2.30, 2.35, 2.40 and 2.46, with the axis connecting initial bubble centres plotted. In the computation, the parameters used are $\varepsilon = 50, R_0 = 0.1911$.

3D coalescence of two bubbles in an oblique configuration for γ_{bb} = 0.6 and δ = 0.5 is shown in Fig. 25. The coalescence occurs at t_* = 0.45 and two slightly curved coalescence surfaces are observed due to the strong buoyancy. At t_* = 1.30 when the maximum volume is reached, the bubble bottom is contracting. As shown in Fig. 25(c) - (f), two jets are formed in the collapse phase. The 1st jet is directed diagonally towards the upper bubble. As the jet evolves, a large vertical deviation occurs. Afterwards, the 2nd jet originates on the bottom surface. At t_* = 2.47, the 1st jet is about to impact the top surface. Compared with the above cases, the upward migration of the coalesced bubble becomes larger with the increase of δ. Fig. 26 shows evolution of the pressure field surrounding the coalesced bubble. As shown in Fig. 26(a), the formation of the 1st jet is due to the high curvature of the bubble surface. Then the strong buoyancy (the pressure gradient) induces the 2nd jet originating on the bottom surface (see Fig. 26(b)). Afterwards, a high-pressure region is produced below the coalesced bubble, which further drives the advancing of the two jets (see Fig. 26(c)). At t_* = 2.47, the pressure peak in the liquid increases and the high-pressure region migrates upward with the bubble. The axis connecting initial bubble centres is also plotted in Fig. 26(d). The 1st jet has a large vertical deviation due to the buoyancy.

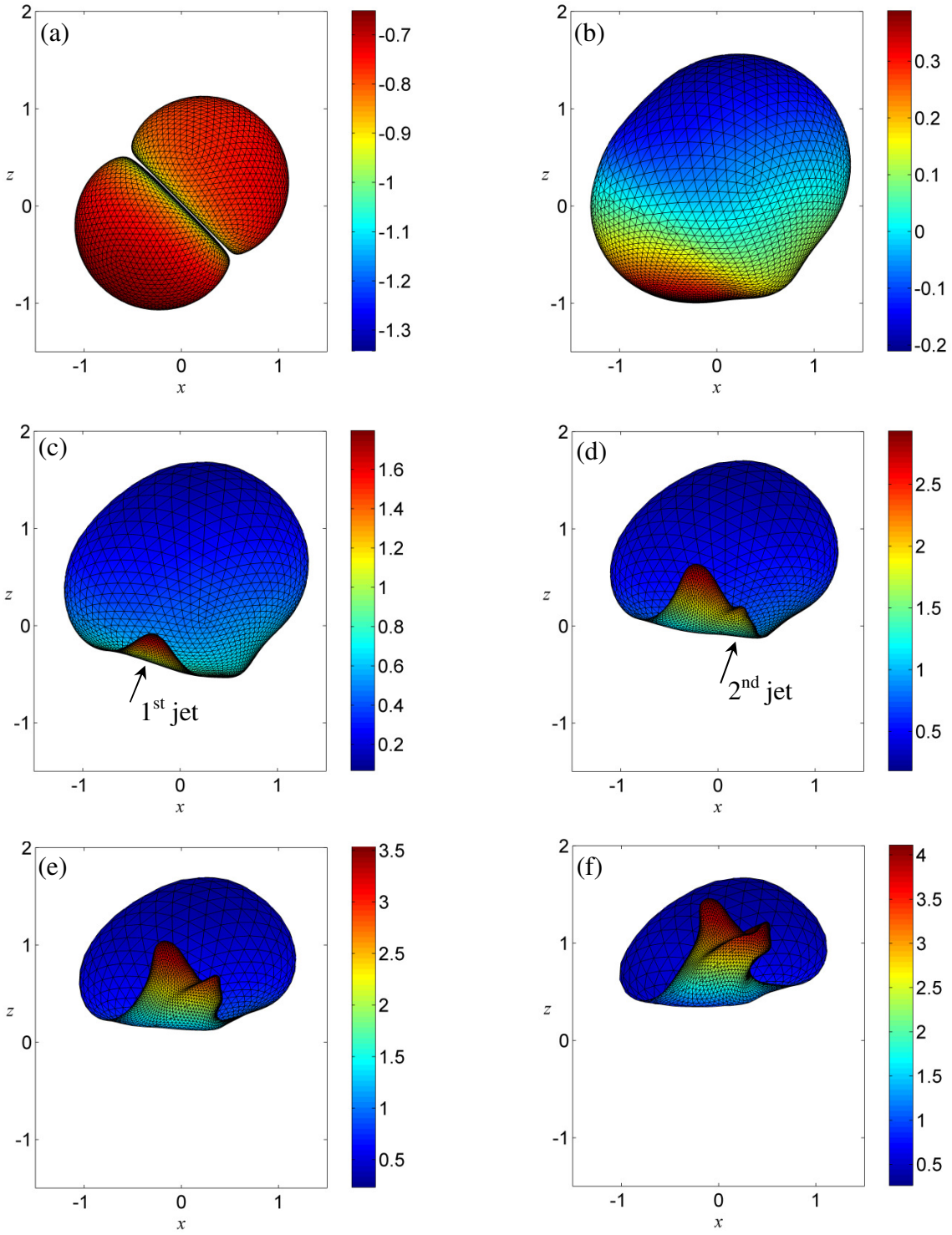

Fig. 25. 3D coalescence of two bubbles in an oblique configuration $\gamma_{bb} = 0.6$ and $\delta = 0.5$. The corresponding time is (a) $t_* = 0.45$, (b) $t_* = 1.30$, (c) $t_* = 1.85$ (d) $t_* = 2.14$, (e) $t_* = 2.30$ and (f) $t_* = 2.47$. In the computation, the parameters used are $\varepsilon = 50, R_0 = 0.1911$.

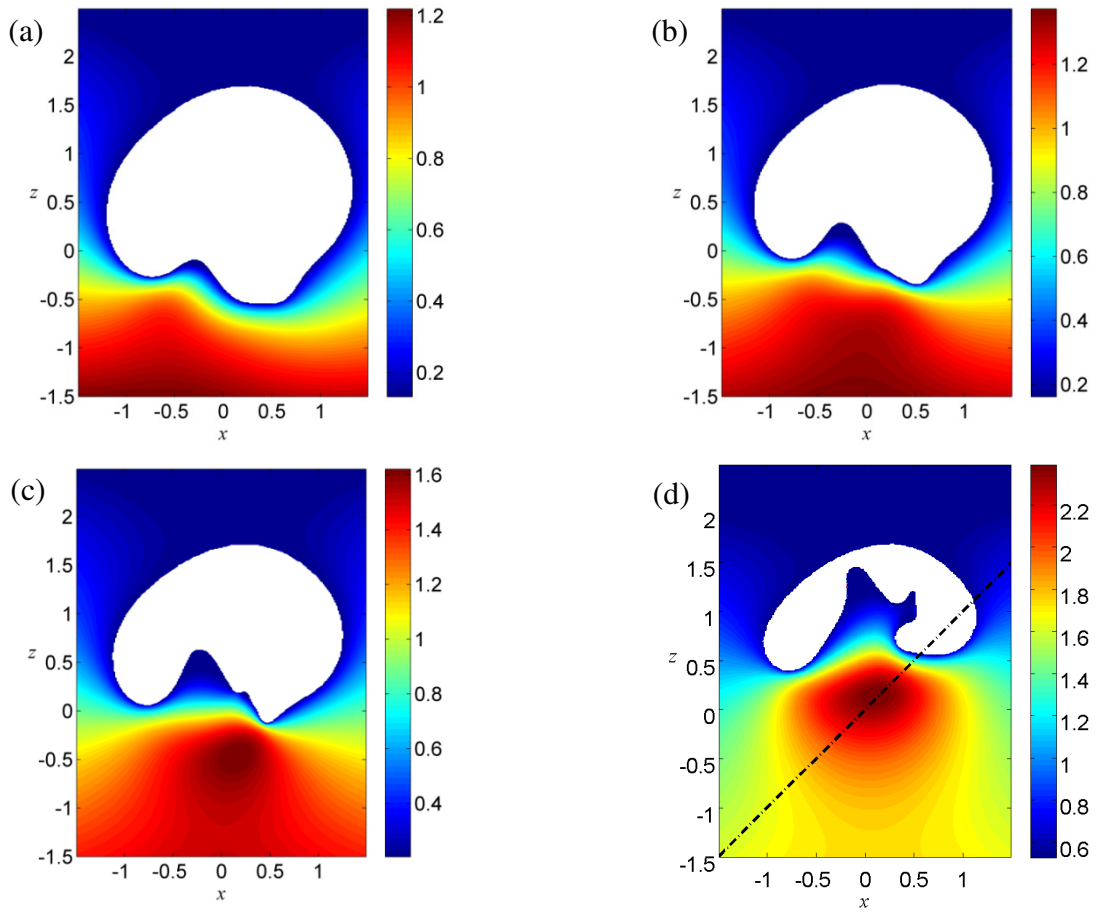

Fig. 26. Pressure field surrounding the coalesced bubble after jet formation, with the parameters the same as in Fig. 25. The corresponding time is (a) $t_* = 1.85$ (b) $t_* = 2.00$ (c) $t_* = 2.14$ and (d) $t_* = 2.47$.

In the coalescence of two bubbles in an oblique configuration, the positions where jets originate move downward along the bubble surface with increasing δ, i.e. they approach to the bubble bottom. The increase of δ greatly affects the upper part where jet originates and delays the occurrence of the jet formation; however, it promotes the jet formation on the lower part. If the buoyancy parameter increases to a certain value (like $\delta = 0.5$), the positions where jets originate may coincide or be too close, so there will be only one jet (as shown in Fig. 25).

The effects of δ on time histories of the total bubble volume and z-component of Kelvin impulse for the bubble system are similar to the above cases (not shown here). Fig. 27(a) shows the centroid trajectories for various δ in the xz-plane. Obviously, the centroid of the bubble system keeps rising due to the buoyancy, and it also moves along the x-axis. In the cases with $\delta = 0.1$ and $\delta = 0.2$, the x-coordinate of the centroid is negative at the jet impact, which means that the centroid migrates towards the lower bubble. While in the case with $\delta = 0.5$, it's the other way around. Time histories of centroid motion of the two bubbles along the x- and z-axis are illustrated in Fig. 27(b) – (c), respectively. In Fig. 27(b), the centroid migrates horizontally

towards the upper bubble during the majority of its lifetime. After $t_* = 2.00$, the centroid moves rapidly in the opposite direction, i.e. a fast horizontal migration of the centroid occurs towards the end of the collapse phase. The reasons are given as follows. In the expansions phase, the presence of buoyancy restrains the motion of the lower parts of the bubble, and the upper parts have higher expanding velocity. Therefore, the centroid motion migrates horizontally towards the upper bubble. In the collapse phase, the lower parts of the bubble collapse faster. The centroid thus continues to move horizontally towards the upper bubble. Towards the end of the collapse phase, the migration of the centroid in the opposite direction is observed. In the cases with $\delta = 0.1$ and $\delta = 0.2$, it's related to the fast contraction of the upper parts and the formation of the 1st jet (see Fig. 23 and Fig. 24). Besides, the formation of the 2nd jet promotes the centroid migration towards the lower bubble. In the case with $\delta = 0.5$, the 2nd jet is formed towards the end of the collapse phase (see Fig. 26(b)), leading to the horizontal migration of the centroid towards the lower bubble. However, the advancing of the 1st jet has a large vertical deviation due to the strong buoyancy, which may retard the horizontal migration towards the lower bubble. In a word, the increasing δ makes the centroid migrate horizontally faster and farther towards the upper bubble during the majority of the bubble lifetime. In Fig. 27(c), the centroid migrates upward faster and farther with increasing δ.

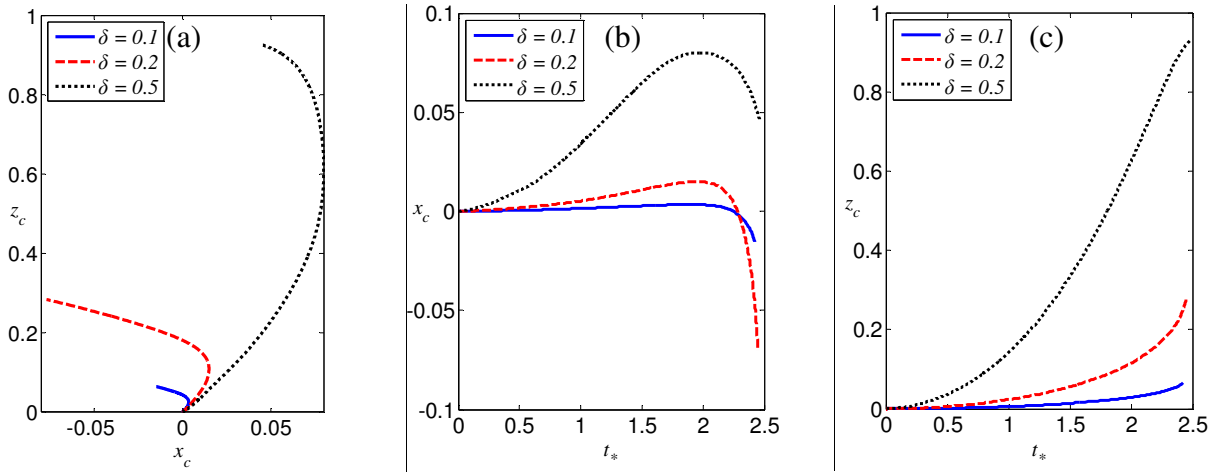

Fig. 27. Effects of buoyancy parameter δ on (a) centroid trajectory in the xz-plane, (b) time history of centroid motion of the two bubbles along the x-axis and (c) time history of centroid motion of the two bubbles along the z-axis. The inter-bubble distance is $\gamma_{bb} = 0.6$.

9. Summary and conclusions

A three dimensional (3D) model has been developed to simulate the coalescence of two bubbles, using the boundary integral method. A high quality surface mesh was maintained, using

a mesh control technique. Our 3D model agrees well with an axisymmetric model for axisymmetric cases and experiments. We analyzed the coalescence of two bubbles of the same size and initiated at the same time in three types of configurations. The interaction and coalescence of two bubbles depend on the dimensionless centre distance γ_{bb} between two bubbles at inception in terms of the maximum bubble radii R_{m}, the buoyancy parameter δ, and the angle β between the centre line and the direction of buoyancy. Some features of coalesecence are observed and the principle conclusions are summarized as follows.

In weak buoyancy cases ($\delta < 0.1$), if two bubbles coalesce during expansion, an elongated bubble is thus formed. Then two jets form on the elongated parts of the coalesced bubble surface during the collapse of the joined bubble.

As the centre line of the two initial bubbles is parallel to buoyancy ($\beta = 0$), the two jets are in contrary direction and their velocities increase with γ_{bb}. The increase of δ promotes the upward jet formation, but delays the downward jet formation. If δ increases to a certain value, only an upward jet is formed. In some cases, the secondary upward jet of the coalesced bubble is observed, leading to a "crown-like" skirt at the base of the jet.

As the centre line of the two initial bubbles is perpendular to bouyancy ($\beta = \pi/2$), the locations where jets originate move downwards and the two jets are inclined to the direction of buoyancy as δ increases. If γ_{bb} increases, the vertical deviation of the two jets becomes larger and the jet impact occurs earlier. Subject to strong buoyancy, a third jet forms directed upwards.

In an oblique configuration ($\beta = \pi/4$), the centroid of the system migrates both upwards and horizontally. It first migrates horizontally towards the upper bubble during the majority of the bubble lifetime but migrates back towards the end of the collapse phase.

In terms of the total bubble volume, δ and γ_{bb} have little effect on the bubble expansion. The increase of δ causes a slower bubble contraction, while the increase of γ_{bb} leads to a faster bubble contraction and an earlier jet impact.

The numerical results in this paper for two-bubble coalescence subjected to strong buoyancy reveal some new phenomena that need to be investigated experimentally in the future.

Acknowledgment

This work is supported by the National Natural Science Foundation of China (51379039), the National Program for Support of Top-notch Young Professionals and the Natural Science Foundation of Heilongjiang Province of China (JC201307).

References

Blake, J.R., Robinson, P. B., Shima, A., Tomita, Y., 1993. Interaction of two cavitation bubbles with a rigid boundary. J. Fluid Mech. 255, 707-721.

Bremond, N., Arora, M., Dammer, S.M., Lohse, D., 2006. Interaction of cavitation bubbles on a wall. Phys. Fluids 18, 121505.

Brennen, C.E., 1995. Cavitation and bubble dynamics. Cambridge University Press.

Chew, L.W., Klaseboer, E., Ohl, S.W., Khoo, B.C., 2011. Interaction of two differently sized oscillating bubbles in a free field. Phys. Rev. 84, 066307.

Cole, R.H., 1948. Underwater Explosion. Princeton University Press, New Jersey.

Cox, E., Pearson, A., Blake, J.R., Otto, S.R., 2004. Comparison of methods for modeling the behaviour of bubbles produced by marine seismic airguns. Geophys. Prospect. 52, 451-477.

Cui, P., Wang, Q.X., Wang, S.P., Zhang, A.M., 2016. Experimental study on interaction and coalescence of synchronized multiple bubbles. Phys. Fluids 28, 012103.

Fong, S.W., Adhikari, D., Klaseboer, E., Khoo, B.C., 2009. Interactions of multiple spark-generated bubbles with phase differences. Exp. Fluids 46(4), 705-724.

Han, B., Köhler, K., Jungnickel, K., Mettin, R., Lauterborn, W., Vogel, A., 2015a. Dynamics of laser-induced bubble pairs. J. Fluid Mech. 771, 706-742.

Han, R., Zhang, A.M., Liu, Y.L., 2015b. Numerical investigation on the dynamics of two bubbles. Ocean Eng. 110, 325-338.

Hsiao, C.T., Choi, J.K., Singh, S., Chahine, G.L., Hay, T.A., Ilinskii, Yu.A., Zabolotskaya, E., Hamilton, M.F., Sankin, G., Yuan, F., Zhong, P., 2013. Modelling single- and tandem-bubble dynamics between two parallel plates for biomechanical application. J. Fluid Mech. 716, 137–170.

Klaseboer, E., Hung, K.C., Wang, C., Wang, C.W., Khoo, B.C., Boyce, P., Debono, S., Charlier, H., 2005. Experimental and numerical investigation of the dynamics of an underwater explosion bubble near a resilient/rigid structure. J. Fluid Mech. 537, 387-413.

Lal, M.K., Menon, S, 1996. Interaction of two underwater explosion bubbles. ASME Fluids Engineering Division Conference, FED, 236 (1), 595-600.

Lauterborn, W., 1982. Cavitation bubble dynamics-new tools for an intricate problem. Appl. Sci.

Res. 38, 165-178.

Li, S., Han, R., Zhang, A.M., Wang, Q.X., 2016. Analysis of pressure field generated by a collapsing bubble. Ocean Eng. 117, 22-38.

Mitchell, T.M., Hammitt, F.G., 1973. Asymmetric cavitation bubble collapse. J. Fluids Eng. 95(1), 29-37.

Rungsiyaphornrat, S., Klaseboer, E., Khoo, B.C., Yeo, K.S., 2003. The merging of two gaseous bubbles with an application to underwater explosions. Comput. Fluids 32, 1049-1074.

Sussman, M., Smereka, P., Osher, S., 1994. A level set approach for computing solutions to incompressible two-phase flow. J. Comput. Phys. 114, 146-205.

Sussman, M., Fatemi, E., 1999. An efficient, interface-preserving level set redistancing algorithm and its applications to interfacial incompressible fluid flow. SIAM J. Sci. Comput. 20, 1165-1191

Tomita, Y., Shima, A., Sato, K., 1990. Dynamic behavior of two laser-induced bubbles in water. Appl. Phys. Lett. 57(3), 234-236.

Vogel, A., Lauterborn, W., Timn, R., 1989. Optical and acoustic investigations of the dynamics of laser-produced cavitation bubbles near a solid boundary, J. Fluid Mech. 206, 299-338.

Wang, C., Khoo, B.C., Yeo, K.S., 2003. Elastic mesh technique for 3D BIM simulation with an application to underwater explosion bubbles. Comput. Fluids 32(9), 1195-1212.

Wang, Q.X., 2005. Unstructured MEL modelling of unsteady nonlinear ship waves, J. Comput. Phys. 210(1), 632-658.

Wang, Q.X., Manmi, K., 2014. Three dimensional microbubble dynamics near a wall subject to high intensity ultrasound, Phys. Fluids 26, 032104.

Zhang, A.M., Cui, P., Wang, Y., 2013. Experiments on bubble dynamics between a free surface and a rigid wall, Exp. Fluids 54(10), 1-18.

Zhang, A.M., Liu, Y.L., 2015. Improved three dimensional bubble dynamics model based on boundary element method, J. Comput. Phys. 294, 208-223.

Zhang, Y.L., Yeo, K.S., Khoo, B.C., Wang, C., 2001. 3D jet impact and toroidal bubbles, J. Comput. Phys. 166, 336-360.